

Bi-abundance photoionization models of planetary nebulae: determining the amount of Oxygen in the metal rich component

V. Gómez-Llanos[★] and C. Morisset[†]

Instituto de Astronomía (IA), Universidad Nacional Autónoma de México, Apartado postal 106, C.P. 22800 Ensenada, Baja California, México.

Accepted XXX. Received YYY; in original form ZZZ

ABSTRACT

We study the hypothesis of high metallicity clumps being responsible for the abundance discrepancy found in planetary nebulae between the values obtained from recombination and collisionally excited lines. We generate grids of photoionization models combining cold metal-rich clumps emitting the heavy element recombination lines, embedded in a normal metallicity region responsible for the forbidden lines. The two running parameters of the grid are the metallicity of the clumps and its volume fraction relative to the whole nebula. We determine the density and temperatures (from the Balmer jump and the [O III] 5007/4363 Å line ratio), and the ionic abundances from the collisional and recombination lines, as an observer would do. The metallicity of the near-to-solar region is recovered, while the metallicity of the clumps is systematically underestimated, by up to 2 orders of magnitude. This is mainly because most of the H β emission is coming from the "normal" region, and only the small contribution emitted by the metal-rich clumps should be used. We find that a given ADF(O⁺⁺) can be reproduced by a small amount of rich clumps, or a bigger amount of less rich clumps. Finally, comparing with the observations of NGC 6153 we find 2 models that reproduce its ADF(O⁺⁺) and the observed electron temperatures. We determine the fraction of oxygen embedded in the metal-rich region (with a fraction of volume less than 1%) to be roughly between 25% and 60% of the total amount of oxygen in the nebula (a few $10^{-3} M_{\odot}$).

Key words: planetary nebulae: general – planetary nebulae: individual: NGC 6153 – methods: numerical – ISM: abundances

1 INTRODUCTION

Determining the physical properties and chemical abundances of the interstellar medium can help us to get a better understanding about the formation and evolution of galaxies. Photoionized regions such as planetary nebulae (PNe) and H II regions, give us information about the past and the present composition of the interstellar medium in which they were formed. The method for estimating chemical abundances in these regions is well detailed in Peimbert et al. (2017). However, there are two big problems in the determination of physical parameters and chemical abundances in photoionized regions. The first problem is that in most

cases the temperature T(BJ) estimated using the Balmer jump of H is lower than the temperature T([O III]) determined with the emission line ratio [O III] 4363/(4959+5007) (Peimbert 1971). The second problem is that the ionic abundances estimated with optical recombination lines (ORLs) are systematically higher than the ones estimated with collisionally excited lines (CELs) for the same ion. The ratio of these two ionic abundances is defined as the abundance discrepancy factor (ADF). Liu et al. (2001b) shows that there is a positive correlation between the ADF(O⁺⁺) and the difference in temperatures T([O III])-T(BJ) for a sample of 11 PNe. Tsamis et al. (2004) show that there is some evidences for a cold plasma using the ORLs observations. Some mechanisms have been proposed to explain the abundance discrepancy, such as temperature fluctuations in the gas (Peimbert 1967), non-thermal electron energy distribution (Nicholls et al. 2012), density condensations (Vie-

[★] E-mail: <mailto:vgomez@astro.unam.mx>, ORCID: <https://orcid.org/0000-0002-1825-8267>

[†] E-mail: <mailto:chris.morisset@gmail.com>, ORCID: <https://orcid.org/0000-0001-5801-6724>

gas & Clegg 1994), and abundance inhomogeneities (Torres-Peimbert et al. 1990; Liu et al. 2000; Péquignot et al. 2002).

Chemically homogeneous photoionization models of PNe can not reproduce both CELs and ORLs in the cases of high ADFs (Bohigas 2009). Models combining chemically inhomogeneous regions have been able to reproduce the CEL and ORL simultaneously (Péquignot et al. 2002; Tylenda 2003; Ercolano et al. 2003; Tsamis & Péquignot 2005, 2006, for the cases of NGC 6153, M 2-36, M 1-42, Abell 30, 30 Doradus, and PN SMC N87). Afterward, a 3D chemically inhomogeneous model developed by Yuan et al. (2011) for the PN NGC 6153, with an ADF \sim 10, successfully reproduces the observed intensities of the CELs and ORLs. In this chemically inhomogeneous model, the H-poor (or metal-rich) region that only has less than 2% of the total mass contributes to the majority of the emission of heavy elements ORLs, while the emission of UV and optical CELs of heavy elements comes mainly from the gas with "normal" metallicity. If the amount of metals in the H-poor region increases, the emissivity of the ORLs will be higher. The same line emission could then be obtained with a more massive and not so metal-rich region or a less massive and more metal-rich region, leading to a degeneracy between the metallicity of the metal-rich region and its mass contribution.

Observational evidence of chemical inhomogeneities has been shown by García-Rojas et al. (2016), where narrow-band images of PN NGC 6778 are obtained. The images show that the regions emitting the ORLs O II 4649+51 is located in the central parts of the nebula, while the CEL [O III] 5007 comes from the outer parts of the nebula that coincides with the H α emission. Peña et al. (2017) measured the expansion velocity (V_{exp}) for different ions using ORLs and CELs, for 14 PNe, finding that in most cases the kinematics is different for ORLs and CELs ($V_{exp}^{ORLs} < V_{exp}^{CELs}$). They suggest that the ORLs are emitted by a plasma that was ejected in a different event than the plasma emitting the CELs, causing the difference in expansion velocities.

An important parameter when chemical inhomogeneities are present, is the electronic temperature of the H-poor region, since it can give us an idea of how H-poor is the gas. However, determining this temperature it is not an easy task, given that ORLs have a low dependence on temperature, and are very faint. Small uncertainties in the recombination line ratios will give a large variations in the temperature estimation.

In this work we want to investigate the ADF values (determined as an observer would do) for models composed of different metallicity regions: a gas with "normal" metallicity and a metal-rich gas. We study the degeneracy between the metallicity and the mass of the metal-rich gas, and the consequences of the overestimation of H β when determining abundances with ORLs. We show that the total mass of oxygen involved in the metal-rich region is not strongly affected by the degeneracy and we determine a range of values for this parameter in the case of PN NGC 6153.

The structure of the paper is outlined here. In sect. 2 we describe how we make the models, its components and the hypothesis that are assumed. In sect. 3 we show the estimations of plasma physical conditions and chemical abundances for the outputs of the bi-abundance models. In sect. 4 we compare the results of our models to an observed object. In sect. 5 we discuss the obtained results and detail

the limitations of the work. Finally in sect. 6 we present the conclusions of the work.

2 MODELING STRATEGY

We use the code Cloudy v.17.02 (Ferland et al. 2017), via the python library pyCloudy (Morisset 2013), to compute the photoionization models for this work. This code solves the thermal equilibrium, the photoionization equilibrium and the radiative transfer for each concentric cell in a spherical symmetric simulation. The code outputs the electron temperature and density, the ionic fractions of all the elements, as well as the line emission for each cell of the model. The line emissions are obtained with PyNeb (Luridiana et al. 2012) in the case of: O II from Storey et al. (2017), and C II and N II from Péquignot et al. (1991). We use the `add_emis_from_pyneb` method from the CloudyModel class of the pyCloudy library, which use the electron temperature and density, and the ionic abundance of the corresponding element, to compute the emissivities of lines which are not computed by Cloudy. It calls the PyNeb corresponding RecAtom class and computes the emission of the lines for each zone of the Cloudy model. The total intensity is obtained by integrating over the volume, in the same way than it is done for the lines computed by Cloudy itself.

To simulate a PN one needs to describe the properties of the ionizing star and its surrounding gas. We simplify the emission of the central star to a black body at a given effective temperature (T_{eff}) and luminosity (L). The gas is described with the following properties: its morphology, its metallicity and its density distribution. We assume a spherical morphology with constant hydrogen density in the whole nebula. In the figure 1 the different regions of the modeled PN are schematically represented in different colors. The nebula is made of a close to solar metallicity gas represented in blue with different darkness (see below) and some metal-rich clumps shown in red. To model such a chemically inhomogeneous nebula with a 1D photoionization code, we actually run different models that will be combined afterward. One model (M_1) corresponds to the "normal" gas (N , middle darkness blue in Fig. 1). Another model (M_2) deals with the metal-rich clumps (MR , in red) and the gas behind these clumps (BC , light blue). This model M_2 is in fact computing 2 regions at once. It appears that in some conditions this BC gas recombines at a smaller radius than the N gas outer radius: this implies the existence of a fourth region: a shadowed component (S , in dark blue of fig. 1) of same metallicity than the N component, that requires its own model (M_3).

As a summary we present in table 1 the names of the different components, their corresponding abbreviations, the reference of the photoionization model, and the regime of metallicity for each one of the four components. These four gas components are detailed in the following sections.

2.1 "Normal" (N) component

The "normal" (N) region is the base component (with close to solar metallicity) of our nebular models. We choose to compare our models with the PN NGC 6153 (see section

Table 1. Some properties of the four components used to build the PN model in this work.

Name	Abbreviation	Model	Metallicity
"normal"	<i>N</i>	M_1	close to solar
meta-rich	<i>MR</i>	M_2	rich
behind clump	<i>BC</i>	M_2	close to solar
shadow	<i>S</i>	M_3	close to solar

2.6), because it has UV, optical and IR observations (Pottasch et al. 1984; Liu et al. 2000) and a previous 3D bi-abundance model has been published by Yuan et al. (2011, here after Y11). The parameters for the *N* component are based on the Bn component of the 3D bi-abundance model by Y11. From the column of the Bn component of their table 2, we take the effective temperature (92 kK), luminosity (1.3×10^{37} erg/s) and chemical abundances (shown in table 2). The inner and outer radius of our *N* component are approximated to 5 and 15 arcsec based on the observations and models presented in Y11. The distance to NGC 6153 used by Y11 is of 1.5 kpc (Péquignot et al. 2003), but more recent data has been published by Gaia Collaboration (2018) resulting in distance of 1.36 kpc. With such a distance the inner and outer radius of the nebula are 1.02×10^{17} cm and 3.05×10^{17} cm, respectively. The hydrogen density is simplified to a constant value of $3,000 \text{ cm}^{-3}$, taken as an approximation of the the density distribution of Y11. The $H\beta$ flux from the model with the described parameters is compared to the observed value of NGC 6153, finding that the $H\beta$ flux in the model is about twice the observed one. To lower the $H\beta$ flux to about half in the same physical size, we add a filling factor (ff) and diminish the hydrogen density (nH). The adopted ff is 0.6 and the nH explored are: 1000, 1500, 2000, and 2500 cm^{-3}). We find the best fit of $H\beta$ with an hydrogen density of 2500 cm^{-3} with filling factor of 0.6. In this model the ionization stage (measured with line ratios such as $[S \text{ III}]/[S \text{ II}]$ y $[O \text{ III}]/[O \text{ II}]$) is too high, to fix this we lower the luminosity (to 1.07×10^{37} erg/s) by a factor equal to the square of the ratio of the distances 1.36 (Gaia Collaboration 2018) and 1.5 kpc (Péquignot et al. 2003). Since the ionization stage was still slightly higher, we refine the fit by decreasing the luminosity to 9×10^{36} erg/s. With this parameters the total $H\beta$ flux and ionization stage are simultaneously fitted. We include graphite and silicate dust grains, each following a -3.5 slope size distribution with ten sizes from $0.005 \mu\text{m}$ to $0.25 \mu\text{m}$; the total dust to gas ratio is 4.2×10^{-3} by mass (about 2/3 of the canonical dust for ISM in Cloudy), see Sec. 4 for detailed justification.

The gas modeled here will be referred to as the *N* component, it has the main contribution in terms of mass in the bi-abundance model (see section 2.5). The electron temperature, density and the ionic fraction of H^+ , He^+ , He^{++} , O^+ , O^{+2} and O^{+3} of the different components are shown as a function of depth in figure 2. In particular, solid lines are drawing the behaviour of the *N* component generated by the model M_1 . At depth $\sim 6 \times 10^{16}$ cm we can see the small drop in electronic density (upper right panel) corresponding to the recombination of He^{++} .

Table 2. Chemical abundances of the *N* region in units of $12 + \log(X/H)$.

He = 11.00	Al = 6.45	Ti = 4.95
B = 2.70	Si = 7.54	V = 3.93
C = 8.50	P = 5.41	Cr = 5.64
N = 8.58	S = 7.24	Mn = 5.43
O = 8.75	Cl = 5.37	Fe = 6.18
F = 4.56	Ar = 6.46	Co = 4.99
Ne = 8.25	K = 5.03	Ni = 6.22
Na = 6.24	Ca = 6.34	Cu = 4.19
Mg = 7.58	Sc = 3.15	Zn = 4.56

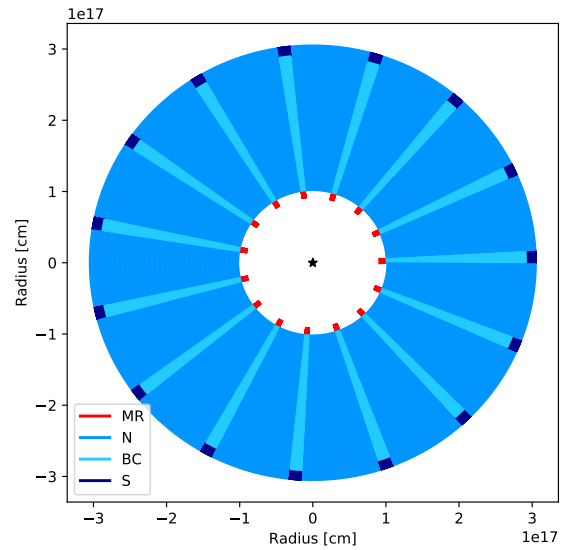


Figure 1. Schematic representation of the morphology of the 4 components of our chemically inhomogeneous PN. All blue regions are gas with close to solar metallicity, and the red regions represents metal-rich (*MR*) clumps that in this case are about 630 times more metallic. The region of middle darkness blue is the "normal" gas (*N*), the light blue region is the gas behind the clumps (*BC*), and the dark blue region is a shadow (*S*) ionized by the diffuse of the normal component. The fraction of solid angle for: *MR*, *BC* and *S* is $\Omega/4\pi = 0.25$.

2.2 Metal-rich (MR) component

The metal-rich (*MR*) component can be seen as a collection of clumps in the inner parts of the nebula. Given the large amount of free parameters, we decided to fix the inner and outer radius of the clumps at $4.5''$ and $5''$ (or 9.2×10^{16} cm and 1×10^{17} cm at a distance of 1.36 kpc), respectively. We only vary the fraction of volume that is occupied by the clumps (but see the Sec. 5 where we explore different values for the density and the inner radius of this *MR* region). The effective temperature, the hydrogen density and the helium abundance are the same than in the *N* component. Tylenda (2003) did a 2-component model of NGC 6153 and found that a better fit is obtained when both components have similar densities. The *MR* and *N* regions are not supposed to be in contact and then not pressure equilibrium hypothesis

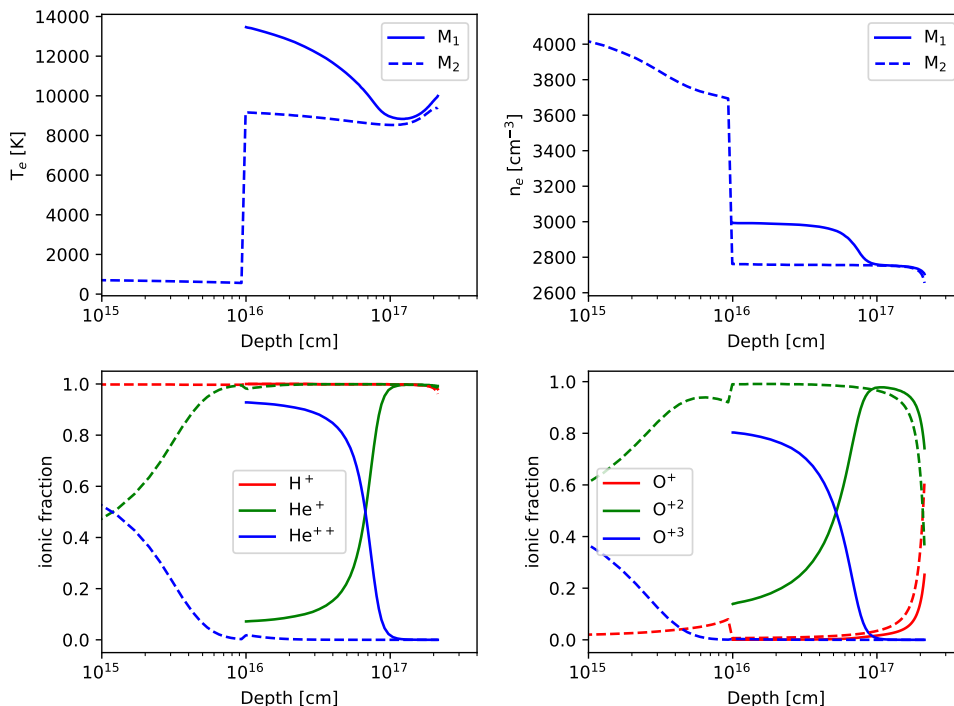


Figure 2. Solid line is for model M_1 that represents the N component (sec. 2.1) and dashed line is for model M_2 that represents: the MR component with $\log ACF = 2.1$ (sec. 2.2) and the BC component (sec. 2.3). The parameter depth is the radius of the model minus the inner radius of the MR component. Top left panel: electron temperature as a function of depth. Top right panel: electron density as a function of depth. Bottom left panel: ionic fraction of H^+ , He^+ and He^{++} in red, green and blue, respectively. Bottom right panel: ionic fraction of O^+ , O^{+2} and O^{+3} in red, green and blue, respectively.

is used. The mean ionization parameter¹ in this region is $\log \langle U \rangle \sim -1.6$. The abundances we adopt for the metals are detailed below.

For a given element X , the abundance in the MR region is defined by the following equation:

$$X/H_{MR} = X/H_N \cdot ACF(X) \quad (1)$$

where $ACF(X)$ is the abundance contrast factor between the N and the MR components. In the following we will mainly use the 10-logarithmic value of the ACF (expressed in "dex"). The enhancement of the abundance in the MR clumps is certainly not uniform (it may differ from one element to another one), but it is out of the scope of this paper to take this effect into account. Thus for a given ACF , the same factor is applied to all the metals. The dust content included in the close-to-solar components (N , BC and S) is less than the canonical D/G for the ISM. The IR emission from this regions reproduces the IRAS observations (see sec. 4.2), so we don't include dust in the MR region, assuming all the dust is in the close-to-solar gas. The opposite extreme assumption that all the dust is in the MR component is discussed in sec. 5.2.

In the figure 2, the MR component is drawn as dashed lines and corresponds to depth $\leq 9 \times 10^{15}$ cm. Its temperature

(upper-left panel) is close to 650 K in this case ($ACF = 2.1$ dex). The electron density (upper-right panel) is higher than in the N component, due to the contribution of the metallic ions to the free electrons soup.

The ionization structure of a given element is determined by the balance between recombination and ionization, with the more ionized ions being closer to the ionization source. In the lower-right panel of figure 2 we can see that at the inner part of model M_2 , where the MR component is present, the dominant ion is O^{+2} , while for the model M_1 of the N component, the dominant ion at the inner part is O^{+3} . Although the ionization source is the same for both models, the O/H abundance is not the same, being 2.1 dex larger for the MR component (in this example) making the amount of photons with energies larger than 54.9 eV not enough for the O^{+3} to be the dominant ion in the MR component. We can see that just before the region of the M_2 model where the abundance goes back to the same value than in the N component (at depth 9×10^{15} cm), the O^+ abundance begins to increase while the O^{+2} and O^{+3} are decreasing, because of the large absorption of photons with energies larger than 35 eV. The decrease in the metal abundances at this transition zone has an abrupt effect on the structure of the oxygen ionization, with an abrupt increase of the O^{+2} ions, and a decrease of the O^+ ions.

In order to confirm that the decrease of O^{++} is due to the lack of 35 eV we show in fig. 3 the total optical depth at the outer radius of the MR component as a function of energy. We clearly see the effect of the metals dominating

¹ $U(r) = Q_0/4\pi r^2 N_e c$, where Q_0 is the ionizing photon rate of the central star per second, r is the distance to the central star, N_e is the electron density and c the light velocity. The mean value is obtained over the volume of the nebula: $\langle U \rangle = \int U dV/V$.

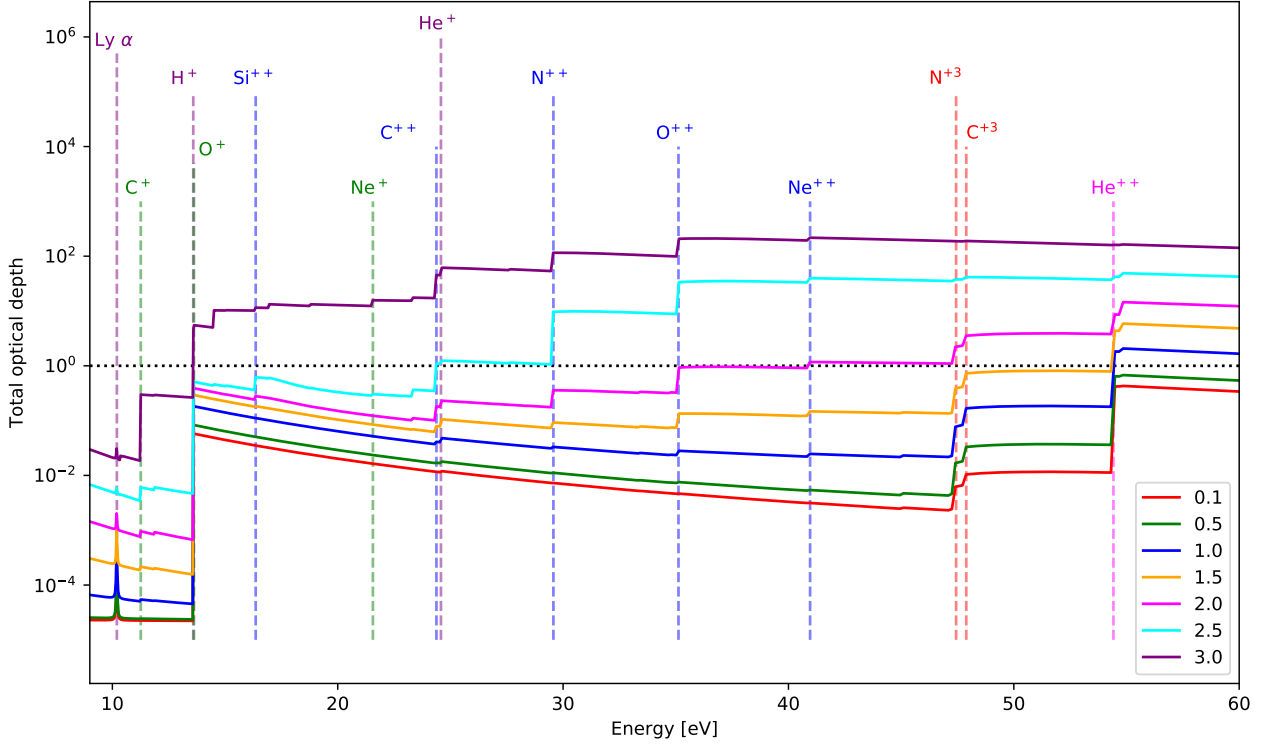


Figure 3. Total optical depth as a function of energy. This value is measured at the outer radius of the *MR* component for ACF(X): 0.1, 0.5, 1.0, 1.5, 2.0, 2.5 and 3.0 dex. The horizontal black dotted line indicates the optical depth equal to 1. The vertical dashed lines denote ionization potentials, for H and He: purple (magenta) represents once (twice) ionized ions, for metals: the colors green, blue and red are for once, twice and three times ionized ions respectively.

the changes in the optical depth at high metallicities. We can see that for $\text{ACF} \gtrsim 2.0$ dex the optical depth starts to be larger than 1 at 35 eV.

To illustrate this behaviour in more details, we show the ionic fractions (integrated over the volume) of oxygen as a function of the ACF(O) in the top panel of fig. 4. When the ACF increases, we observe a decrease of the mean ionization of the *MR* region. We fixed the size of this region, which is then matter-bounded (we consider here only the *MR* region. There is actually close to solar metallicity gas behind this region, it will be discussed in sec. 2.3). Increasing the metallicity increases the opacity of the gas, reducing its Strömgren size. In the case of the smallest metallicity, the relatively small *MR* region only includes the inner part of what would be the *MR* region if not matter-bounded, corresponding to the highest ionization. On the other side, when the metallicity is very high, the *MR* region is almost radiation-bounded and shows a global lower ionization.

2.3 Behind clumps (*BC*) component

Behind the *MR* component we found gas with the same chemical abundances and dust than the *N* component but with a different ionization stage, we will call this gas “behind clump” (*BC*) gas. Cloudy is able to model the *BC* region in the same run than the *MR* region. So for each *MR* gas a *BC* gas will be modeled, in the same run. We use the *function* command of Cloudy, to include dust only in the *BC* component of the model. The model including the *MR* and *BC*

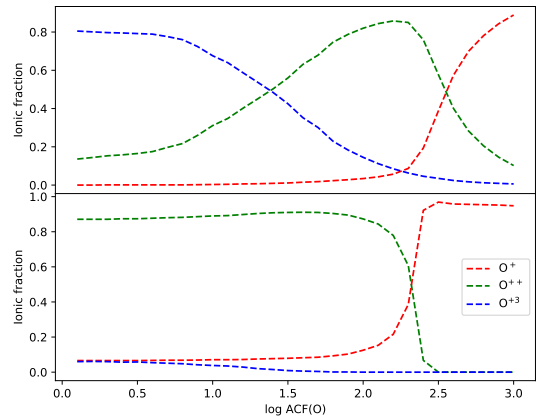


Figure 4. Distribution of the ionic fraction integrated over the volume of O^+ , O^{++} , and O^{+3} in red, green and blue dashed lines, respectively, as a function of the $\log \text{ACF}(\text{O})$ for the *MR* component in the top panel, and the *BC* component in the bottom panel.

components will be referred to as the M_2 model. The *BC* component has the same hydrogen density, chemical abundances and inner radius than the normal component but a different outer radius and ionization parameter since the *MR*

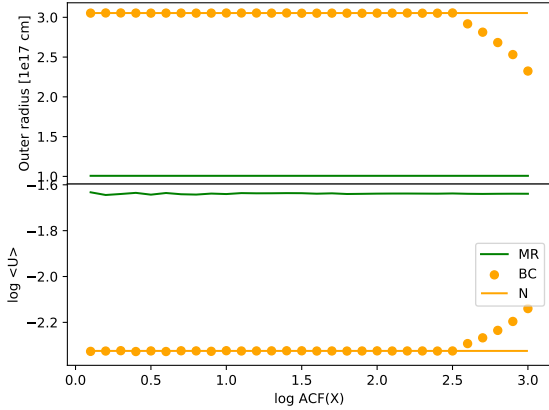


Figure 5. The top panel represents the outer radius as a function of the log ACF(X) for: the *MR*, *BC* and *N* components as a solid green line, orange dots and solid orange line, respectively. The bottom panel represents the log of the mean ionization parameter as a function of log ACF(X) for: the *MR*, *BC* and *N* components as a solid green line, orange dots and solid orange line, respectively.

gas that is at a smaller radius than the *BC* gas is absorbing some of the ionizing radiation.

In the bottom panel of fig. 4 we show the *BC* component ionic fractions of oxygen integrated over the volume as a function of the ACF(O). We can see that at log ACF \sim 2.3 the dominant ion changes from O^{++} to O^+ . For values of ACF smaller than 2.3 dex, there is still some photons more energetic than 35 eV entering the *BC* region and ionizing all the O^+ . Above 2.3 dex, no more photons ionizing O^+ escape the *MR* region, and the *BC* region is purely O^+ . This will have an effect in the contribution of the O^{++} emission coming from the *BC* region for ACF $>$ 2.3 dex.

The outer radius and the mean ionization parameter of the *BC* gas are shown as a function of the ACF(X) in figure 5, for comparison the outer radius and the mean ionization parameter of the *N* component are also shown. We notice that when the ACF(X) reaches values of 2.6 dex, the *BC* gas starts to recombine at a smaller radius than the outer radius of the *N* component. The size of the *BC* regions starts to decrease, leading to an increase of the mean ionization parameter $\langle U \rangle$ (lower panel of fig. 5). The space between the recombination front of the *BC* region and the outer radius of the nebula is then filled by the shadow region (see Sec. 2.4).

2.4 Shadow (*S*) component

Since the models M_1 and M_2 are combined to form a spherical morphology, when the model M_2 recombines at a smaller radius than M_1 , there is a shadow after M_2 . The ionization of the shadow is due to the diffuse radiation (mainly Lyman recombination photons) coming from the *N* gas around it. We build a model (M_3) to get an approximate idea of the physical conditions and the emission of the shadow (*S*) region. We use one single model for all the shadow regions obtained with different values of ACF(X), this model has the same abundances and dust content than the *N* component. We use as representative ionizing flux the nebular

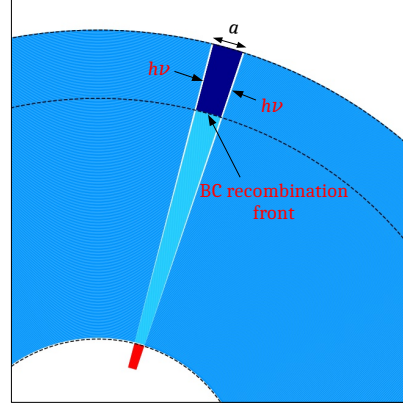


Figure 6. Colors represent the same regions as in figure 1. Scheme characterizing the parameters of the *S* region. The outer part of the *S* region has an arch size of a , the $h\nu$ arrows represent the direction of the diffuse ionizing photons coming from the *N* region to ionize the *S* region.

continuum computed by Cloudy during the M_1 model, at the radius corresponding to half of the nebula. The figure 6 gives a schematic representation of the shadow region in dark blue. The shadow region is what follows the recombination front of the *BC* region. We are actually computing a model where the radial direction of the Cloudy 1D model corresponds to the tangential direction of our object (illustrated by the “ $h\nu$ ” arrows in Fig. 6). The radial size of the *S* regions are determined by the difference in radius between the recombination front of the *BC* region and the outer radius of the *N* region (see fig. 5). On the other side, the tangential size (a in Fig. 6) of the clumps (the depth of the Cloudy model) needs to be defined.

As we are only interested in the representative emission produced by the *S* ionized region, we will adopt a value for this size a that avoid a neutral tube inside the *S* region. To obtain this result, we cut the Cloudy model at the half of its Strömgen size. The electron temperature of this region is almost constant and close to 6300 K. The electron temperature of the surrounding material (*N* region) is 30% higher than this value; this could imply a higher density for the *S* region in case of pressure equilibrium. We did not took this effect into account, keeping the hydrogen density at the same value in all the regions.

2.5 Bi-abundance models

We combine the three models M_1 , M_2 and M_3 described in the previous sections to obtain the emission of the whole nebula. The parameter we use to define the fraction of volume each model occupies is the solid angle (Ω) of the *MR* region (and the *BC* and *S* regions).

We actually do not perform a 3D model, not even a pseudo-3D models *a la* Gesicki et al. (2016). We rather add the intensities computed by each models using a weight determined by Ω .

In this combined model the intensity of a line is obtained

with the following equation:

$$I(\lambda) = I(\lambda)_{M_1} \left(1 - \frac{\Omega}{4\pi}\right) + I(\lambda)_{M_2} \left(\frac{\Omega}{4\pi}\right) + I(\lambda)_{M_3} \left(\frac{\Omega}{4\pi}\right) \quad (2)$$

where $I(\lambda)_{M_i}$ is the intensity at the wavelength λ for model M_i as computed by Cloudy for a 4π sphere. In the case of M_3 , the intensity $I(\lambda)_{M_3}$ already takes into account the thickness of the shadow which depends on the position of the BC recombination front.

It is almost topologically equivalent to use a single model with $\Omega/4\pi$ or a collection of n clumps, each one with an angular size of $\Omega/(4\pi n)$. This is not totally the case for the S region: a large clump may lead to a neutral tube in its shadow, while a smaller clump will have a fully ionized shadow. We choose to model the shadows without neutral component, imposing an implicit upper limit of the clump sizes.

In the following sections we will explore the effect of the metallicity enhancement (ACF) and the contribution of the MR (and BC and S) component. This is achieved by considering a grid of models where ACF ranges from 0.1 to 3.0 dex by 0.1 dex steps, and $\Omega/4\pi$ ranges from 0.01 to 0.5.

2.6 NGC 6153: a reference PN with high ADF

In this section we make a brief summary of the observations taken from the literature that are used to compare with our models.

NGC 6153 is an intrinsically bright PN located in the southern sky at a distance of 1.36 kpc (Gaia Collaboration 2018), it has an angular size of $32'' \times 30''$ (Skrutskie et al. 2006, NIR). It was observed with the ESO 1.52 m telescope by Liu et al. (2000). They used the B&C spectrograph, the slit was 2 arcsec wide and 3.5 arcmin long. The spatial sampling was 1.63 arcsec per pixel. A "minor-axis" of the PN was observed by placing the slit in a PA of 122.8° centered in the central star. The mean spectra of the whole nebula was obtained scanning across the nebula with a long-slit oriented north-south. A high resolution spectra (FWHM = 1.5\AA) was obtained for the spectral range $\lambda\lambda 3995\text{-}4978\text{\AA}$, and a low resolution spectra (FWHM = 4.5\AA) in the spectral range $\lambda\lambda 3535\text{-}7400\text{\AA}$. The observations were corrected for bias, flats, cosmic rays, they were wavelength calibrated with an He-Ar calibration lamp. The flux was calibrated using standard stars, and dereddened using the galactic extinction curve of Howarth (1983) with $c(H\beta)=1.30$ and $R = 3.1$. Liu et al. (2000) determined the chemical abundances for NGC 6153 and an $ADF(O^{++})$ of 9.2.

3 PLASMA DIAGNOSTICS WITH THE MODEL OUTPUTS

The emission of the bi-abundance models (see 2.5) are used as a simulation of a real PN (with equation 2), to determine the physical parameters and chemical abundances with the same methods than for a real object. The results are shown in the following subsections. The electronic temperature and density, and the ionic abundances are determined using the code PyNeb version 1.1.9 (Luridiana et al. 2013). The atomic data used for each ion are listed in table 3, if the electronic

temperature is under 500 K (the case for the MR component at very high ACF) an extrapolation is made to the H I recombination coefficients from Storey & Hummer (1995).

3.1 Physical parameters with CELs

The line emissions are obtained from the bi-abundance models using eq. 2, for the grid of ACF and $\Omega/4\pi$ explored. As we are mainly interested by the medium ionization zone ($20 \text{ eV} < IP < 45 \text{ eV}$), we determine the temperature and the density simultaneously using the line ratios: [O III] 4363/5007 \AA and [Cl III] 5538/5518 \AA . The contribution of recombination to the [O III] 4363 line is naturally included in the models, no correction from this effect has been performed (but see the Sec. 5.3 for a discussion of the [O III] 4363 emission). The results are shown in figure 7, where the x-axis represents the changes in the ACF, the y-axis represents the changes in $\Omega/4\pi$ and the color represents the electronic temperature (density) in the top (bottom) panels respectively. Both parameters are found almost constant in the ACF- Ω plane, with variations of less than 5% and 10% for electronic density and temperature, respectively. This is due to the fact that they are determined using CEL which are mainly emitted by the close to solar components (N , BC and S regions). Small variations appear in the high ACF-high Ω corner of the plots. In the case of the temperature, it may seem counter-intuitive that the temperature increases in the case of a higher contribution of the cold MR region. What we see here is the effect of the contribution of the recombination to the [O III] 4363 emission, coming from the MR region, which increases at low temperatures. The strong change in the temperature at $\log ACF \sim 2.2$ is due to the sudden vanishing of O^{++} emission in the BC region (see sec. 2.3). The decrease of the temperature at constant Ω and high values of ACF is due to the increase of the contribution of the S region to the emission of [O III] 5007.

3.2 Electronic temperature from the Balmer Jump

The electronic temperature can also be estimated from the Hydrogen Balmer jump normalized to a Balmer line (Peimbert 1967). For the ACF- Ω grid, we estimate the Balmer jump temperature, $T(BJ)$, using the Continuum class from PyNeb. The method requires: the flux of the continuum (in units $\text{erg}\cdot\text{s}^{-1}\text{cm}^{-3}\text{\AA}^{-1}$) at a wavelength previous and latter to the Balmer jump (such wavelengths can be defined by the user, we choose 3643 and 3861 \AA), a line intensity of H (in units $\text{erg}\cdot\text{s}^{-1}\text{cm}^{-3}$, we choose H11), the electronic density and the He^+/H^+ and $\text{He}^{++}/\text{H}^+$ abundances ratios. As an observer would do, we use for the electron density the estimation obtained from a density diagnostic, here the [Cl III] 5538/5518 \AA line ratio, as derived in the previous section (bottom panel of fig. 7). In the range of density we are expecting for a PN (lower than 10^5 cm^{-3}), the exact adopted value does not strongly affect the derived temperature. The He^+/H^+ and $\text{He}^{++}/\text{H}^+$ abundances ratios are estimated consistently by iterative process with the $T(BJ)$ using the following lines normalized to $H\beta$: He I 4471, 5876 and 6678 for He^+/H^+ , and He II 4686 for $\text{He}^{++}/\text{H}^+$. The resulting $T(BJ)$ is shown in figure 8. We can see that as metallicities (or

Table 3. Atomic data selected from PyNeb that are used in the determination of physical parameters and chemical abundances.

Collisionally excited lines		
Ion	Transition probabilities	Collision strength
N ⁺	Froese Fischer & Tachiev (2004)	Tayal (2011)
O ⁺	Froese Fischer & Tachiev (2004)	Kisielius et al. (2009)
S ⁺	Podobedova et al. (2009)	Tayal & Zatsarinny (2010)
O ⁺⁺	Froese Fischer & Tachiev (2004) ^a	Storey et al. (2014)
Cl ⁺⁺	Kaufman & Sugar (1986) ^b	Butler & Zeippen (1989)
Ar ³⁺	Mendoza & Zeippen (1982)	Ramsbottom & Bell (1997)
Recombination lines		
Ion	Recombination coefficients	Case
H ⁺	Storey & Hummer (1995) ^c	B
He ⁺	Smits (1996)	B
He ⁺⁺	Storey & Hummer (1995)	B
O ⁺⁺	Storey et al. (2017)	B

^a For transitions 4-2 and 4-3 we use Storey & Zeippen (2000).

^b For transition 4-3 we use Mendoza (1983).

^c We make an extrapolation at low Te (< 500 K).

ACF) and Ω increase, the temperature starts to decrease, mainly because of the contribution of the *MR* component that are cooler at higher metallicity and also because of the contribution of *BC* and *S* components that are at a lower temperature than the *N* component.

3.3 Estimation of O⁺⁺/H⁺ with CELs

We estimate the ionic abundance of O⁺⁺/H⁺ for the ACF- Ω map with the CEL [O III] 5007Å in two ways: taking the T([O III]) for both O⁺⁺ and H⁺, and taking T([O III]) for O⁺⁺ and T(BJ) for H⁺. In figure 9 we show the determination with T(BJ) for H⁺. The other determination that only uses T([O III]) differs by a factor roughly equal to T(BJ)/T([O III]) to what is shown in fig. 9. From fig. 9 we see a 0.3 dex decrease of O⁺⁺/H⁺ at high Ω and ACF larger than 2.3 dex. This is due to the abrupt decrease of O⁺⁺/O from the *BC* region (see bottom panel of fig. 4). In this high ACF regime (> 2.3 dex): at constant ACF when the Ω decreases the contribution of the *BC* region also decreases and at constant Ω when the ACF increases the outer radius of the *BC* region decreases (see top panel of fig. 5). In both cases the contribution in volume of the *BC* region to the total O⁺⁺/H⁺ is smaller. Since there is less (if any) O⁺⁺ in this region (at high ACF) the total O⁺⁺/H⁺ increases again.

The value of $12 + \log O/H$ used in the close to solar components (*N*, *BC* and *S*) is 8.75. The value obtained from the CELs is slightly lower than this value, because of the ionic fraction O⁺⁺/O being lower than one. We also computed the "real" value of O⁺⁺/H⁺ by integrating over the volume of the nebula the contribution of the *N*, *BC* and *S* regions (no contribution from *MR* is taken into account, as this region does not emit [O III] 5007Å), which is close to both empirical determinations, being slightly closer for the T(BJ) estimation.

3.4 Estimation of O⁺⁺/H⁺ with ORLs

We estimate the ionic abundances of O⁺⁺/H⁺ with ORLs for the grid of ACF- Ω explored in the bi-abundance models. Given that the dependence of O II recombination lines to

the electronic temperature is small, we use the Balmer jump temperature estimated in sec. 3.2. We make an average of the abundance determined with the same 3-3 recombination lines of O II than in table 14 of Liu et al. (2000). The O⁺⁺/H⁺ estimation is shown in figure 10. The same calculation was made with the temperature from [O III] 4363/5007 Å, and the results were very similar. We see in fig. 10 changes of 1 order of magnitude from the low ACF-low Ω corner to the high ACF-high Ω opposite corner. At ACF larger than 1 dex the contribution of the *MR* region becomes important given the low temperature of the region, favoring the recombination line emission.

The determination of O⁺⁺/H⁺ from ORLs is expected to provide the actual value of the O⁺⁺/H⁺ in the *MR* region (if H β is dominant in this region). We see here that this is far from being the case at high ACFs, the highest value obtained for $12 + \log O^{++}/H^{+}$ being 9.9 (at $\Omega/4\pi = 0.5$ and ACF(O) = 2.4 dex) while for the *MR* region it reaches 10.8.

3.5 Estimation of the ADF(O⁺⁺)

From the values of O⁺⁺/H⁺ determined from CELs and ORLs (see previous sections) we can compute the ADF(O⁺⁺), which is shown in fig. 11. This can be compared to the ACF(O) running on the x-axis. In almost the whole ACF- Ω plane, the difference is important, reaching a factor of 50 in the upper right corner. For the *MR* component, the ionic fraction O⁺⁺/O is always higher than 0.06 in the ACF- Ω plane, so even though we are comparing the discrepancy factor of O⁺⁺ to the contrast factor of O, this difference can not be completely attributed to the O⁺⁺/O ratio. The value for the close to solar regions determined from the CELs being actually close to the "real" value used as input of the models, the discrepancy is coming from the ORLs determination that does not match the "real" value. The main issue of this determination is not the temperature but rather the estimation of the H β proportion coming from the O II line emitting region (*MR* component) as described in the next section.

We compare in figure 12 the ADF(O⁺⁺) to the ACF(O⁺⁺), defined by the ratio of O⁺⁺/H⁺ integrated over the *MR* region and O⁺⁺/H⁺ integrated over the *N+BC+S*

regions. This can be seen as the measure of the error one do when determining the ADF, the ACF being the "true" value of the ionic abundance difference. Whatever the value of Ω , the log ACF(O) around 0.8 corresponds to a good determination of the ADF (white solid line in fig. 12). For lower values of the ACF(O), the ADF(O⁺⁺) overestimates the value of ACF(O⁺⁺) (by up to 0.7 dex). This corresponds to situations where the contribution to O II coming from the close to solar regions actually dominates the total emission of the O II lines. For values of ACF(O) greater than 0.8 dex, the O II emission mainly comes from the *MR* region and the ADF(O⁺⁺) underestimates the true value given by the ACF(O⁺⁺) by a factor up to ~100 (dark solid line in fig. 12).

3.6 Contributions of the *MR* clumps to recombination lines.

In Figs. 13 and 14 we draw the contribution of some recombination lines (namely for H β and the V1 multiplet of O II) emitted by the *MR* region relative to the total emission. The H β emission is mainly coming from the close to solar components, as the *MR* contribution is never higher than 9%. On the other side, the O II lines are well representative of the *MR* region when this one is strongly H-poor (ACF(O) > 1.5 dex). The apparent incapacity of the O II lines to correctly predict the ACF of the nebula (see previous sections) is actually mainly due to the impossibility to only take into account the H β emitted by the *MR* region.

4 MODELS FITTING A REAL OBJECT

4.1 Looking for solutions for NGC 6153

The two main observables related to the Abundance Discrepancy problem are the value of the ADF and ΔT the difference T([O III]) - T(BJ). We determine this parameters for NGC 6153 (with the same method than for our models), namely ADF(O⁺⁺)=8.2 (using T(BJ)) and $\Delta T=3025$ K (with the observations presented in Liu et al. 2000), to define an area in the ACF- Ω plane where the models fit these values. This area is shown in fig. 15, where the blue (green) color band shows where the model fits ADF(O⁺⁺) (ΔT resp.) within $\pm 15\%$. Another way to perform a similar determination is by plotting the observables predicted by the models, as in fig. 16. The color code corresponds to the values of ACF (right panel) and $\Omega/4\pi$ (left panel). The diamond corresponds to the observations for NGC 6153. Using a box of $\pm 15\%$ around the observed values, we can extract the models and exhibit the values of ACF- Ω combinations that reproduce the observations. This is done in fig. 17. Two families of solutions appear around [ACF(O⁺⁺), $\Omega/4\pi$] = [2.1, 0.50] and [2.8, 0.18]. The best solutions correspond to S₁: a lower ACF but high volume for the *MR* region, and S₂: a higher ACF but smaller volume.

The characteristics of these two solutions are summarized in table 4, where T_e , n_e , the ionic fractions of H⁺, O⁺, O⁺⁺ and O⁺³ and the fractions of volume and mass are given for each one of the 4 regions. The electron temperature of the *N* region is close to 9500 K, while the *BC* and *S* components are at slightly lower temperature. The *MR* region is found to be as cold as 500-600 K. The high value of n_e found

in the *MR* region is due to the contribution of the metals to the free electrons. The ionic fractions indicates that the two solutions are very different in the *MR* - *BC* - *S* regions: the S₁ solution almost does not have *S* region, and the *MR* and *BC* regions are mainly O⁺⁺, while the S₂ solution exhibits a *S* component and show the *MR* and *BC* regions well recombined to O⁺. In both cases, the mass or volume fraction of the *MR* region relative to the whole nebula is rather small.

One interesting result is that despite the fact that both solutions differs by a factor of ~ 4 in the O/H abundance, the mass of oxygen embedded in the *MR* region only differs by a factor of ~ 1.5. This points out that the *MR* oxygen mass is somewhere robust against the degeneracy of the solutions relative to ACF(O) and Ω , each one acting in opposite direction. We then determine the oxygen in the metal-rich region in NGC 6153 to be ~40% of the total oxygen in the nebula, this in a volume that is less than 1%.

These two solutions S₁ and S₂ will be used in the next sections to explore the emission of the corresponding models.

4.2 Emitted spectra

We use the solutions S₁ and S₂ determined in the previous section to show in fig. 18 the contribution to the total emission coming from each one of the 4 regions (in different colors), for a set of 28 representative emission lines. An extensive list of emission lines with the intensity emitted by each region, normalized to H β , for both solutions, is given in table A1.

For both solutions we compare in table 5 the infrared emission to the observed values through the 4 IRAS bands at 12, 25, 60 and 100 μm obtained for PN NGC 6153 from Helou & Walker (1988). We can see that in both solutions the IR emission from the model is very close to the observed emission. For the S₁, the IR band fluxes are well reproduced. For the S₂, the model is higher than the observed fluxes at 12, 25, and 60 μm , and a good fit for 100 μm is obtained. The emission at the shorter wavelengths bands is already higher than what is observed, adding dust to the *MR* component will increase the emission in this range. Thus there is no evidence of the presence of dust in the *MR* region, thus we don't include dust in the *MR* component. This result agrees with what Ercolano et al. (2003) found for the polar knots of Abell 30, but is in contradiction with what Borkowski et al. (1994) found in the case of the equatorial H-poor ring of the same object. The interpretation of this lack of dust in the metal rich region, in terms of creation and destruction of dust, is out of the scope of this paper, nonetheless, the extreme opposite case where all the dust is in the *MR* component is discussed in sec. 5.2.

We see again that the contribution of H β coming from the *MR* region is very small. This is the key problem in the determination of the true value of the *MR* region metallicity, translated in the difference between the ADF (observed) and ACF (real).

The important contribution of the *MR* region coming from the metal recombination lines is clearly seen, as well as from the infrared lines. The contribution of the *BC* and *S* regions are different in the two solutions.

From the table A1 we can see that the total intensities of some lines (latest column) change between the 2 solutions: the C II (N II) recombination lines increase by a factor of ~2.8

Table 4. Physical parameters for each one of the four components, for the two solutions S₁, and S₂ in parenthesis.

	Normal	Rich clumps	Behind clumps	Shadow
$\langle T_e \rangle$ [K]	9536 (9536)	629 (527)	8906 (7252)	7117 (7117)
$\langle n_e \rangle$ [cm ⁻³]	2770 (2770)	3817 (5728)	2738 (2610)	2056 (2056)
12+log(O/H)	8.75 (8.75)	10.85 (11.45)	8.75 (8.75)	8.75 (8.75)
$\Omega/4\pi^*$	0.50 (0.80)	0.50 (0.20)	0.50 (0.20)	0.50 (0.20)
H ⁺ /H	0.99 (0.99)	1.00 (1.00)	0.99 (0.96)	0.74 (0.74)
O ⁺ /O	0.06 (0.06)	0.04 (0.70)	0.15 (0.96)	0.46 (0.46)
O ⁺⁺ /O	0.86 (0.86)	0.84 (0.28)	0.84 (0.00)	0.26 (0.26)
O ⁺³ /O	0.07 (0.07)	0.11 (0.02)	0.00 (0.00)	0.00 (0.00)
O mass (10 ⁻⁴) [M _⊙]	6.6 (10.5)	7.5 (12.3)	6.6 (2.0)	0.0 (1.0)
Volume [10 ⁵⁰ cm ⁻³]	345.1 (554.2)	3.1 (1.3)	345.0 (105.0)	0.5 (51.3)
% mass	49.3 (76.7)	1.4 (1.7)	49.3 (14.5)	0.1 (7.1)

* Fraction of solid angle for each component.

Table 5. Emission from IRAS bands for PN NGC 6153 (Helou & Walker 1988) and the two solutions S₁ and S₂ in Jansky units.

Wavelength	Observations	S ₁	S ₂
12 μm	6.9	7.2	10.3
25 μm	52.1	72.8	107.0
60 μm	120.0	127.7	173.6
100 μm	52.1	40.3	52.0

(1.7), while the Ne II recombination lines decrease by ~ 25%, between the S₁ and the S₂ solutions. This is mainly due to a change in the ionization of the *MR* region. For the same reason we see a difference in the emission of the infrared lines of [N II] and [Ne II]. The other IR lines are from higher charged ions, less affected by the ionization changes in the *MR* regions. The O II recombination lines are not changing, by construction of our solutions based on fitting the observed ADF(O⁺⁺).

The optical CELs are mainly unchanged between the two solutions.

We use a simplistic relation in the way metals are enhanced in the *MR* region (same ACF for all the metals). The real situation may certainly be more complex and these differences in the C II and N II emission between the two solutions can not be used to derive properties related to the oxygen abundance like ACF(O). Nevertheless, the C II, O II, and N II intensities predicted by both models are close to the observed values given by Yuan et al. (2011). This could be seen as an indication that the C:N:O relative abundances used in *MR* region are adequate.

5 DISCUSSION

5.1 Helium abundance in the *MR* component

The material that is responsible for the observed high ADF (> 10) in some PNe is unique and original. It is not a common ISM component. It is very hard to observe as it is blended with "normal" PN gas in the observations. It mainly emits metal recombination lines, and some H recombination lines. The contribution from this component to the total He recombination lines is almost negligible (as well as in the case of HI lines), and barely distinguishable from the "nor-

mal" component emission. The exact He abundance in this *MR* component is then very hard to determine. On the other side, the fact that this component is cold points to a small heating and strong cooling. We explore a variant of the solutions obtained above, where the He/H abundance is also enhanced. The results are presented in details in the Appendix B. An acceptable solution can be found for He/H as high as 6.3, leading to a slight overprediction of the He I line intensities compared to values reported by Yuan et al. (2011). The total amount of oxygen in the whole nebula derived for this solution does not significantly changed compared to what is found in solutions S₁ and S₂.

This result is similar to that of Yuan et al. (2011), where the He abundance is less enhanced than metals in their metal rich region (He/H (*MR*/*NR*) ≈ 5, while O/H (*MR*/*NR*) ≈ 80, from their Tab.2.).

On the other hand, in the case of the model of Abell 30 presented by Ercolano et al. (2003), the He/H abundance is reaching a value as high as 40, while O was determined to be almost in the same amount than H. We have here lower values for O/H (between 0.07 and 0.35) and for He/H (lower than 6.3). The process leading to the H-poor components in these two object seems to be different.

Finally, if we compare with the abundances determined in some nova shells (nova event is not excluded by Wesson et al. (2018) as a proxy for a scenario to these H-poor clumps), one can see that the strong enhancement determined for the C:N:O elements is not associated to an equivalent enhancement in Helium (See e.g. Morisset & Pequignot 1996).

5.2 Dust in the *MR* component

The creation and destruction of dust in the *MR* component is unknown, and due to the lack of spatially resolved IR observations, we cannot constrain the radial distribution of dust. In the previous sections we have assumed that no dust is in the *MR* component, and all the dust necessary to reproduce the IRAS observations is located in the close-to-solar components. Here we explore the opposite case where the dust is only present in the *MR* component, although the reality may be an intermediate solution between both hypothesis. We generate grids of models including dust of graphite and silicate types with two sizes for each: 1 μm and 0.01 μm, we search for the D/G values that have the closest fit to

the IRAS observations. We define the D/G for each model to be proportional to the O/H of the *MR* component. We follow the same procedure searching for solutions that reproduce ΔT and the ACF(O^{++}), like in the figures 16 and 17. In these models, at some point when the ACF increases the dust becomes optically thick ($ACF > 2.7$ dex) and the gas behind the clumps is no longer ionized by the star, becoming a shadow ionized by the Lyman continuum radiation from the *N* component. The solution at "lower" ACF and higher $\Omega/4\pi$ is lost, and only one solution with $ACF = 2.8$ dex and $\Omega/4\pi = 0.27$, marginally reproduces simultaneously ΔT and ACF(O^{++}). For this solution the IR emission at 12, 25, 60 and 100 μm is 10.2, 44.6, 134.8 and 71.4 Jy, close to the observed values (See Tab. 5). For this solution, the D/G by mass is 1.04, which is considerably higher than the canonical value in the ISM of 6.3×10^{-3} . The abundances of the elements trapped in the dust (in log, by number) are: C = -1.21, O = -0.4, Mg = Si = Fe = -1.0. These values of abundances of elements in dusty phase are even higher than the corresponding abundances in the gaseous phase for Mg, Si and Fe, for O is roughly the same amount and for C is about 30% of the gaseous phase. A more detailed modeling of the distribution of dust could be of interest as further work, but additional observations are needed to constrain the free parameters.

5.3 Recombination contribution to auroral lines

The recombination contribution to the auroral lines for [N II] 5755 is taken from Cloudy based on Nussbaumer & Storey (1984), for [O II] 7332 from Cloudy based on Liu et al. (2001a), for [O III] 4363 from Cloudy (version 17.02) using Pequignot et al. (1991) and Nussbaumer & Storey (1984). We see in Fig. 18 that the contribution of the *MR* component to the auroral lines [N II] 5755 and [O II] 7332 emission is not negligible. This is due to the recombination of N^{++} and O^{++} , favored by the low temperature of the *MR* region. In the grid we explored, the most important contributions reach 1/3 of the total auroral emission, for a model with a determined ADF(O^{++}) of ~ 30 . In case of more extreme ADFs, the recombination contribution may even be dominant. In case of higher excitation nebula the recombination of [O III] 4363 may become significant. This is in total coherence with observations from Jones et al. (2016) and García-Rojas et al. (2016) who found the spacial location of the [O III] 4363 emission in coincidence with the O^{++} recombination lines and not with the [O III] 5007 emission. This effect can be amplified when the observation is obtained in the direction of the metal rich region rather than for the whole nebula, which is the case in high spatial resolution observations. Without taking the effect of the recombination into account, one can determine a gradient of temperature increasing toward the central part of the nebula, where the *MR* regions are located. On the contrary, the increase of [O III] 4363 emission is actually related to a very strong decrease of the electron temperature! We will explore the contribution of the recombination to [O III] 4363 in a forthcoming paper (Gomez-Llanos et al. 2020)

5.4 Ionization correction factor for the *MR* region

The results presented in this work are about the ADF(O^{++}). If one is interested in the ADF(O), an Ionization Correction Factor (ICF) needs to be applied. Even in the case of a low ionization nebula where only O^+ and O^{++} are present, these ionic abundances are determined from the [O II] and [O III] lines that are mainly emitted by the close to solar regions (*N*, *BC* and *S*). For the *MR* region where only O^{++} is observed through the O II lines, the ICF(O^{++}) needs to be used. Since the ICF(O^{++}) for ORLs can't be determined, the one derived for the forbidden lines has to be used. From table 4, we see that the ICF(O^{++}) - which is O/O^{++} - is almost the same for the *N*, *MR* and *BC* regions in the S_1 solution (between 1.1 and 1.2). But in the case of the S_2 solution, the ICF(O^{++}) for the close to solar region is close to 1.1, while the ICF(O^{++}) that needs to be applied to O^{++} in the *MR* region is 4.8.

If the density of the *MR* region, or its radial size, is changed, the ionization of the region will change, and so will the ICF(O^{++}).

The He II 4686 emission is classically used to determine the ICF(O^{++}) taking into account the presence of O^{+3} (Delgado-Inglada et al. 2014). But we see that in the case of the S_1 solution, 20% of the intensity of this line comes from the *MR* region and should be removed before computing the ICF.

5.5 Effects of density and size of the *MR* region

We explored in the previous sections the behaviour of a grid of models. In this grid some parameters have been fixed to reasonable values. This is the case of the *MR* region density, its distance to the central star and its radial size.

The electron density of the *MR* region is hard to constrain by observations: recombination lines (the only ones emitted by this cold region) have quite low dependency on the density. There is no indication that a pressure equilibrium must exist between the warm and the cold regions, as they are not supposed to be in contact. We adopted then the same hydrogen density as for the *N*, *BC* and *S* regions. Increasing for example the density of the *MR* region would increase its optical depth, decreasing its global ionization and possibly leading to a vanishing of the *BC* region, replaced by a pure shadow region.

The effect of changing the radial size of the *MR* region, decreasing for example its inner radius, would lead to a very similar effect: increasing its optical depth.

In both cases, the global emission of the *MR* region, for a given Ω , will increase. To recover the same ADF and ΔT , a lower ACF will be needed for a given Ω .

We performed test cases to explore the effect of changing the hydrogen density and the inner radius of the *MR* component. In a first test, we explore the density range from $1 \times 10^3 \text{ cm}^{-3}$ to $4 \times 10^3 \text{ cm}^{-3}$. At lower densities the models fitting the observed ADF(O^{++}) and ΔT , as shown in fig. 16, have higher Ω eventually reaching impossible values higher than 1. On the other side, at higher densities no solution is found that reproduces simultaneously the ADF(O^{++}) and ΔT .

The other test varying the inner radius between $4.3''$

and $4.7''$, leads to a similar behaviour. A smaller inner radius needs less Ω to fit the two observables.

These tests show that the main result obtained in the previous section is still valid when changing some of the parameters we fixed *a priori* in our grid of models: the ACF (the real metal enhancement of the rich region) is higher than the ADF determined from observations.

From the exploration of this grid, we determine the mass of oxygen embedded in the metal rich clumps to be between 25% and 60% of the total mass of the nebula.

Another limitation of our study is the reality of the *BC* and *S* regions. The very simplistic model presented here assumes a very sharp separation between the *N* region and what is happening behind the *MR* region. Some observations exhibit cometary tails (see e.g. O'Dell et al. 2005, in the Helix nebula) that are very aligned in the direction of the central star. On the other side, the image of NGC 6153 does not show clear evidences of this kind of structure.

6 CONCLUSIONS

In the previous sections we described how a grid of models is obtained considering two metallicity models when varying the abundance of a metal-rich (*MR*) component and its volume. The ratio between the two metallicities is called the Abundance Contrast Factor (ACF). We explored how the physical parameters and chemical abundances can be determined from the observables produced by the models, especially the [O III] and O II emission lines leading to the determination of O^{++}/H^+ by two methods. These two values are classically used to define the Abundance Discrepancy Factor (ADF(O^{++})).

We show that the determination of the ADF(O^{++}) does not represent a good estimation of the ACF(O) given as input of the models, even taking into account that the ACF is defined for the oxygen element and the ADF only for the O^{++} ion. The difference between the ACF and the ADF can be as high as two orders of magnitude. The main limitation is coming from the fact that the ionic abundance O^{++}/H^+ determined from the O II region is computed using the H I intensity resulting from the emission of the whole nebula, when only a small fraction is actually coming from the *MR* region (a maximum of 8% is found in the models we present here).

It is today almost impossible to isolate the contribution of the *MR* region from the total H I emission by observations. Very high spatial and/or spectral resolution observation may solve this important issue.

Nevertheless, we show that it is possible to determine an estimation of the mass of metals (at least oxygen in our case) embedded in the rich component, from the optical recombination lines.

The models reproduce the Infrared observations without needs of an enhanced dust content in the metal rich region.

ACKNOWLEDGEMENTS

We thank the anonymous referee for helping to improve the quality of this research, especially on the discussion of

the presence of dust in the models, and the He/H abundance in the *MR* region. We are very grateful to Grazyna Stasińska and Jorge García-Rojas for reading and helpfully commenting the draft of this paper. This work was supported by CONACyT-CB2015 254132, DGAPA/PAPIIT-107215, and DGAPA/PAPIIT-101220 projects. VGL acknowledges the support of CONACyT and PAEP-UNAM grants. The manuscript of this paper has been written in the Overleaf environment.

DATA AVAILABILITY

The models presented in the paper are available under request to the authors.

REFERENCES

- Bohigas J., 2009, *Rev. Mex. Astron. Astrofis.*, 45, 107
- Borkowski K. J., Harrington J. P., Blair W. P., Bregman J. D., 1994, *ApJ*, 435, 722
- Butler K., Zeppen C. J., 1989, *A&A*, 208, 337
- Delgado-Inglada G., Morisset C., Stasińska G., 2014, *MNRAS*, 440, 536
- Ercolano B., Barlow M. J., Storey P. J., Liu X., Rauch T., Werner K., 2003, *MNRAS*, 344, 1145
- Ferland G. J., et al., 2017, *Rev. Mex. Astron. Astrofis.*, 53, 385
- Froese Fischer C., Tachiev G., 2004, *Atomic Data and Nuclear Data Tables*, 87, 1
- Gaia Collaboration 2018, *VizieR Online Data Catalog*, p. [I/345](#)
- García-Rojas J., Corradi R. L. M., Monteiro H., Jones D., Rodríguez-Gil P., Cabrera-Lavers A., 2016, *ApJ*, 824, L27
- Gesicki K., Zijlstra A. A., Morisset C., 2016, *A&A*, 585, A69
- Gomez-Llanos V., Morisset C., Garcia-Rojas J., Jones D., Wesson R., Corradi R. L. M., Boffin H. M. J., 2020, The impact of strong recombination on temperature determination in planetary nebulae ([arXiv:2007.05488](#))
- Helou G., Walker D. W., 1988, in *Infrared astronomical satellite (IRAS) catalogs and atlases. Volume 7*.
- Howarth I. D., 1983, *MNRAS*, 203, 301
- Jones D., Wesson R., García-Rojas J., Corradi R. L. M., Boffin H. M. J., 2016, *MNRAS*, 455, 3263
- Kaufman V., Sugar J., 1986, *Journal of Physical and Chemical Reference Data*, 15, 321
- Kisielius R., Storey P. J., Ferland G. J., Keenan F. P., 2009, *MNRAS*, 397, 903
- Liu X.-W., Storey P. J., Barlow M. J., Danziger I. J., Cohen M., Bryce M., 2000, *MNRAS*, 312, 585
- Liu X., et al., 2001a, *MNRAS*, 323, 343
- Liu X., Luo S., Barlow M. J., Danziger I. J., Storey P. J., 2001b, *MNRAS*, 327, 141
- Luridiana V., Morisset C., Shaw R. A., 2012, in *IAU Symposium*. pp 422–423
- Luridiana V., Morisset C., Shaw R. A., 2013, *PyNeb: Analysis of emission lines*, *Astrophysics Source Code Library* (ascl:1304.021)
- Mendoza C., 1983, in Flower D. R., ed., *IAU Symposium Vol. 103, Planetary Nebulae*. pp 143–172
- Mendoza C., Zeppen C. J., 1982, *MNRAS*, 198, 127
- Morisset C., 2013, *pyCloudy: Tools to manage astronomical Cloudy photoionization code*
- Morisset C., Pequignot D., 1996, *A&A*, 312, 135
- Nicholls D. C., Dopita M. A., Sutherland R. S., 2012, *ApJ*, 752, 148
- Nussbaumer H., Storey P. J., 1984, *Astronomy and Astrophysics Supplement Series*, 56, 293

- O'Dell C. R., Henney W. J., Ferland G. J., 2005, *AJ*, **130**, 172
- Peña M., Ruiz-Escobedo F., Rechy-García J. S., García-Rojas J., 2017, *MNRAS*, **472**, 1182
- Peimbert M., 1967, *ApJ*, **150**, 825
- Peimbert M., 1971, *Boletín de los Observatorios Tonantzintla y Tacubaya*, **6**, 29
- Peimbert M., Peimbert A., Delgado-Inglada G., 2017, *PASP*, **129**, 082001
- Pequignot D., Petitjean P., Boisson C., 1991, *A&A*, **251**, 680
- Péquignot D., Amara M., Liu X., Barlow M. J., Storey P. J., Morisset C., Torres-Peimbert S., Peimbert M., 2002, in W. J. Henney, J. Franco, & M. Martos ed., *Revista Mexicana de Astronomía y Astrofísica Conference Series Vol. 12*, *Revista Mexicana de Astronomía y Astrofísica Conference Series*. pp 142–143
- Péquignot D., Liu X., Barlow M. J., Storey P. J., Morisset C., 2003, in S. Kwok, M. Dopita, & R. Sutherland ed., *IAU Symposium Vol. 209, Planetary Nebulae: Their Evolution and Role in the Universe*. p. 347
- Podobedova L. I., Kelleher D. E., Wiese W. L., 2009, *Journal of Physical and Chemical Reference Data*, **38**, 171
- Pottasch S. R., et al., 1984, *ApJ*, **278**, L33
- Ramsbottom C. A., Bell K. L., 1997, *Atomic Data and Nuclear Data Tables*, **66**, 65
- Skrutskie M. F., et al., 2006, *AJ*, **131**, 1163
- Smits D. P., 1996, *MNRAS*, **278**, 683
- Storey P. J., Hummer D. G., 1995, *MNRAS*, **272**, 41
- Storey P. J., Zeippen C. J., 2000, *MNRAS*, **312**, 813
- Storey P. J., Sochi T., Badnell N. R., 2014, *MNRAS*, **441**, 3028
- Storey P. J., Sochi T., Bastin R., 2017, *MNRAS*, **470**, 379
- Tayal S. S., 2011, *ApJS*, **195**, 12
- Tayal S. S., Zatsarinny O., 2010, *ApJS*, **188**, 32
- Torres-Peimbert S., Peimbert M., Pena M., 1990, *A&A*, **233**, 540
- Tsamis Y. G., Péquignot D., 2005, *MNRAS*, **364**, 687
- Tsamis Y. G., Péquignot D., 2006, in Stanghellini L., Walsh J. R., Douglas N. G., eds, *Planetary Nebulae Beyond the Milky Way*. p. 192, doi:10.1007/3-540-34270-2_25
- Tsamis Y. G., Barlow M. J., Liu X., Storey P. J., Danziger I. J., 2004, *MNRAS*, **353**, 953
- Tylenda R., 2003, in Kwok S., Dopita M., Sutherland R., eds, *IAU Symposium Vol. 209, Planetary Nebulae: Their Evolution and Role in the Universe*. p. 389
- Viegas S. M., Clegg R. E. S., 1994, *MNRAS*, **271**, 993
- Wesson R., Jones D., García-Rojas J., Boffin H. M. J., Corradi R. L. M., 2018, *MNRAS*, **480**, 4589
- Yuan H., Liu X., Péquignot D., Rubin R. H., Ercolano B., Zhang Y., 2011, *MNRAS*, **411**, 1035

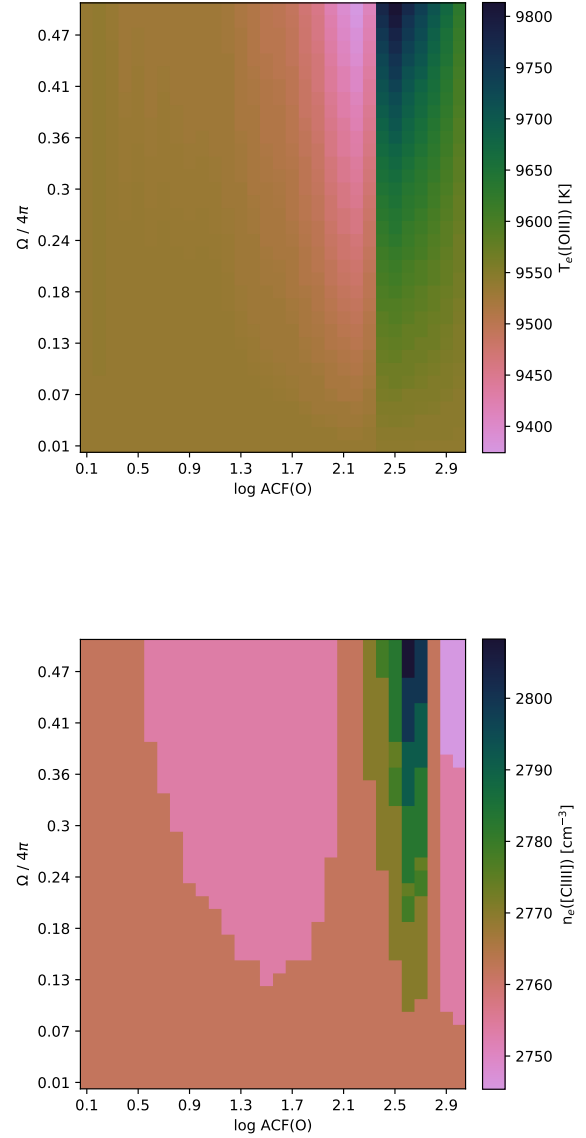


Figure 7. Top (bottom) panel: the color represents the electronic temperature (density) estimation for the bi-abundance models (see sec. 2.5). The x-axis represents the variations in the ACF for oxygen (see eq. 1) and goes from 0.1 to 3.0 dex. The y-axis represents the normalized solid angle of: the metal-rich clumps, the gas behind the clumps and the shadow, in the range of 0.01 to 0.50. Diagnostics are made with the sensitive line ratios: $[\text{O III}]$ 4363/5007 Å and $[\text{C III}]$ 5538/5518 Å. The contribution of recombination in $[\text{O III}]$ 4363 Å is taken into account. Line intensities of the bi-abundance models are obtained using eq. 2.

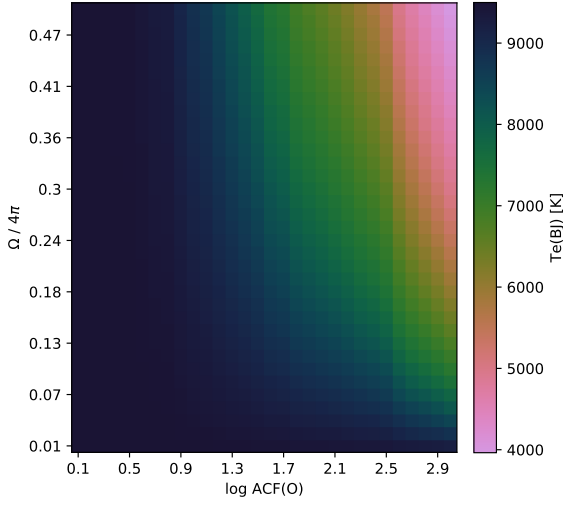


Figure 8. Same axis as figure 7. The color represents the Balmer jump temperature determination for the bi-abundance models.

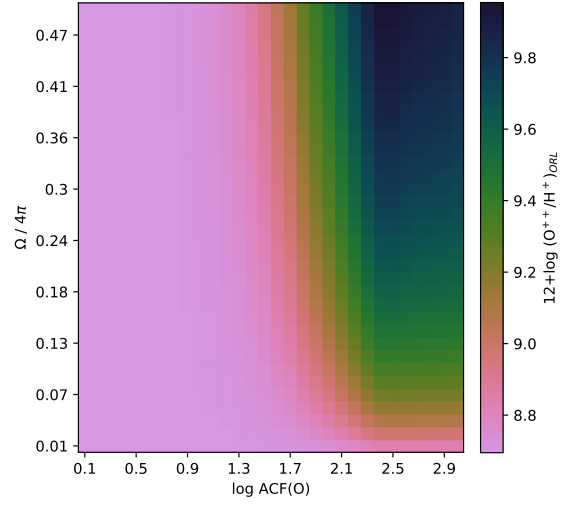


Figure 10. Same axis as figure 7. The color represents the O^{++}/H^+ ionic abundance estimation with ORLs for the bi-abundance models, using the $T(\text{BJ})$ (shown in fig. 8).

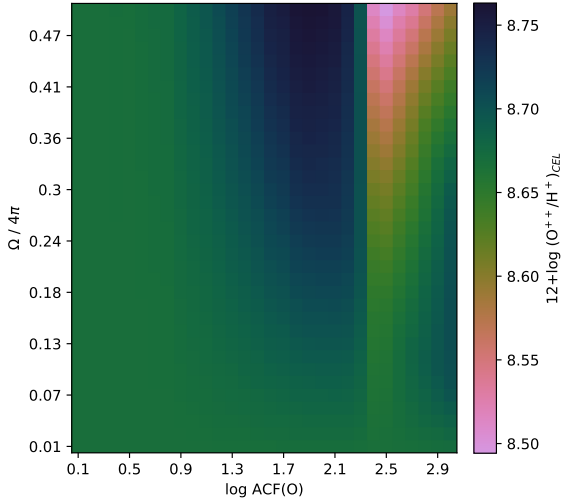


Figure 9. Same axis as figure 7. The color represents the O^{++}/H^+ ionic abundance estimation with CELs for the bi-abundance models, using the $[\text{O III}]$ temperature for O^{++} (shown in top panel of fig. 7), and the Balmer jump temperature (shown in fig. 8) for H^+ .

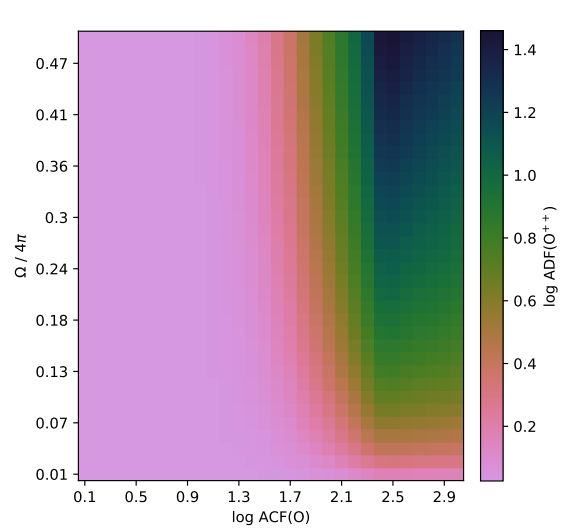


Figure 11. Same axis as figure 7. The color represents the $\log \text{ADF}(\text{O}^{++})$ determined for the bi-abundance models.

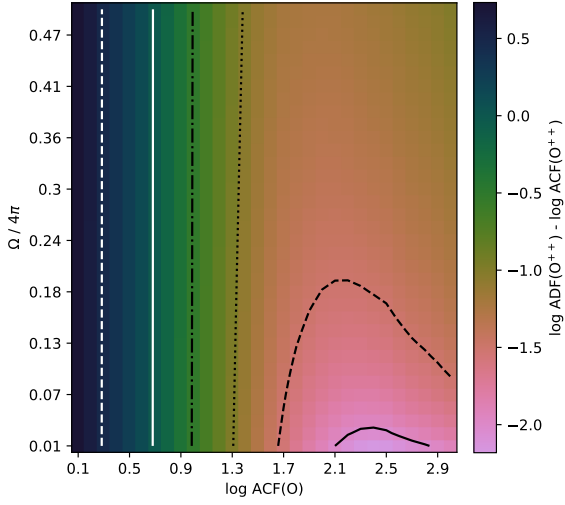


Figure 12. Same axis as figure 7. The color represents the difference in log of the $ADF(O^{++})$ determined for the bi-abundance models and the $ACF(O^{++})$ (difference in O^{++} of the MR and the N , BC and S components). White dashed (solid) is for $\log ADF(O^{++}) - \log ACF(O^{++})$ equal to 0.5 (0.0) and black dash-dotted, dotted, dashed and solid lines are for: -0.5, -1.0, -1.5, -2.0, respectively.

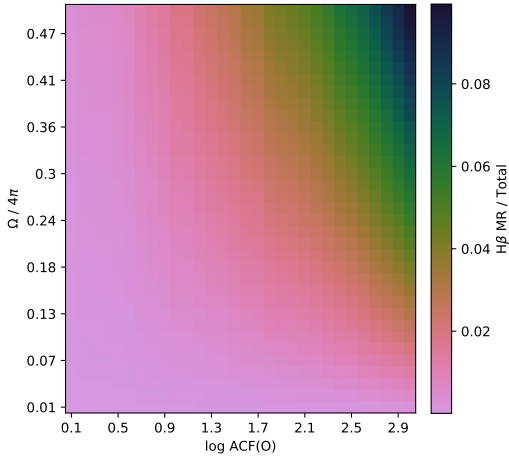


Figure 13. Same axis as figure 7. The color represents the fraction of the $H\beta$ from the clumps to the total emission for the bi-abundance models.

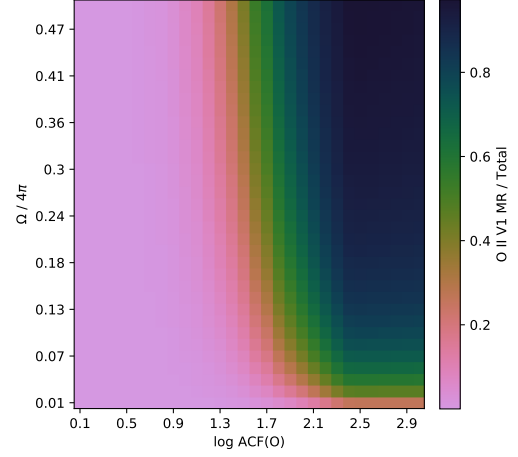


Figure 14. Same axis as figure 7. The color represents the fraction of the V1 multiplet of $O II$ from the MR to the total emission for the bi-abundance models.

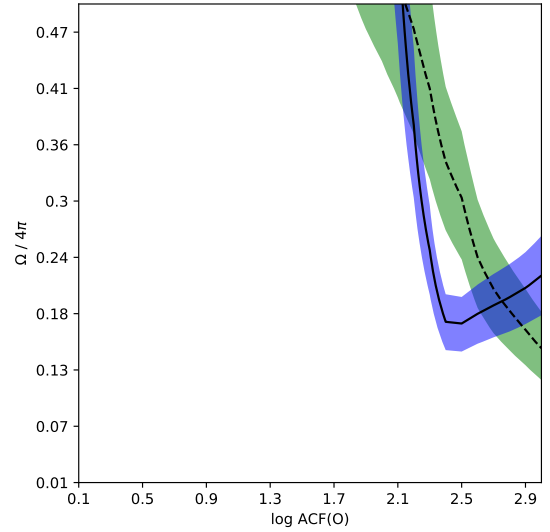


Figure 15. Same axis as figure 7. The black dashed (solid) line represents the bi-abundance models with estimations of $\Delta T = T([O III]) - T(BJ)$ ($ADF(O^{++})$) equal to the observed value of 3025 K (8.2) for NGC 6153 (our determination using the observations from Liu et al. 2000), the green (blue) contours are for 15% above and below this value.

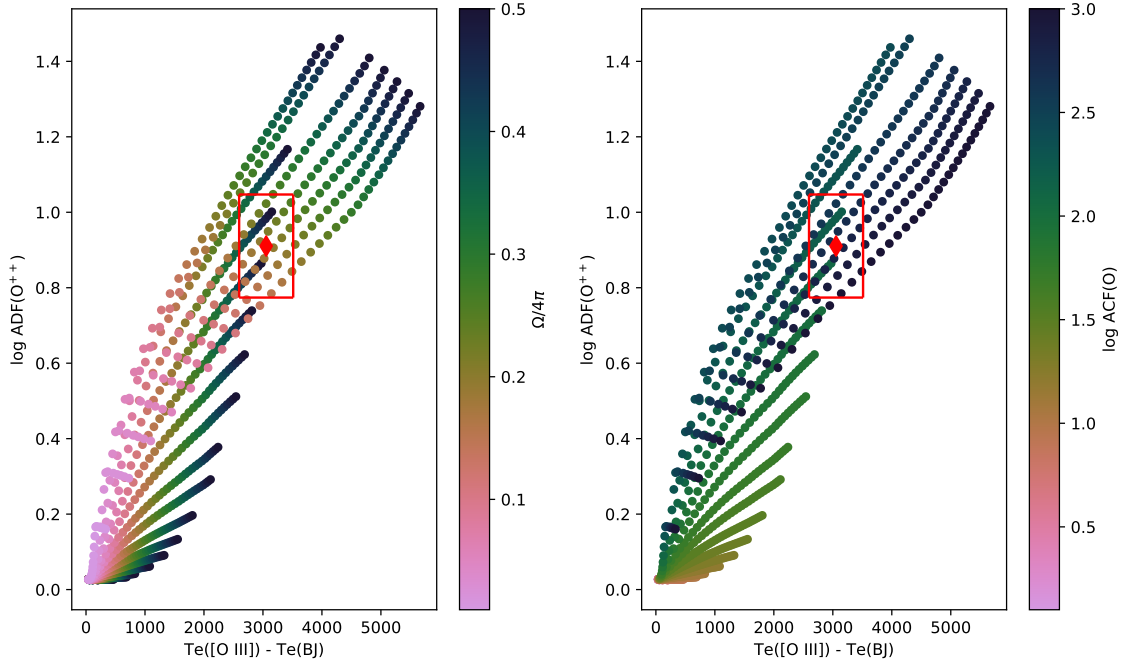


Figure 16. Left panel: color represents the normalized solid angle of: the metal-rich clumps, the gas behind the clumps and the shadow, in the range of 0.01 to 0.50. Right panel: color represents the variations in the ACF for oxygen (see eq. 1) and goes from 0.1 to 3.0 dex for the bi-abundance models. The x-axis shows the difference in temperature estimated with: [O III] 4363/5007 Å and the Balmer jump. The y-axis shows the log ADF(O⁺⁺) estimated for the bi-abundance models. The red diamond represents the value for the PN NGC 6153 taken from Liu et al. (2000) (for the minor axis in the case of Te(BJ) and for the whole nebula in the case of Te([O III]) and ADF(O⁺⁺)). The red square represents the region selected for the models that are closer to the observed value in NGC 6153.

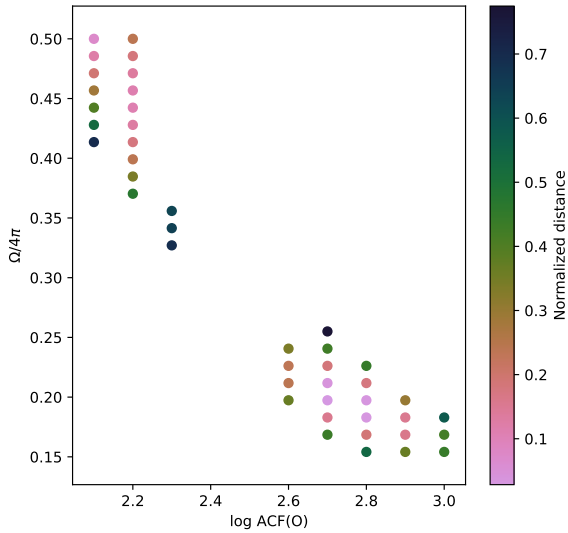


Figure 17. Selected models, as being inside the red square of figure 16. The color represents the distance from the model to the observed value represented as a red diamond in fig 16. The distance ($\sqrt{(x/x_0)^2 + (y/y_0)^2}$, where $x = T([O III]) - T(BJ)$, $y = ADF(O^{++})$) is normalized through x_0 and y_0 so the distance from the centre of the square to a corner is 1.

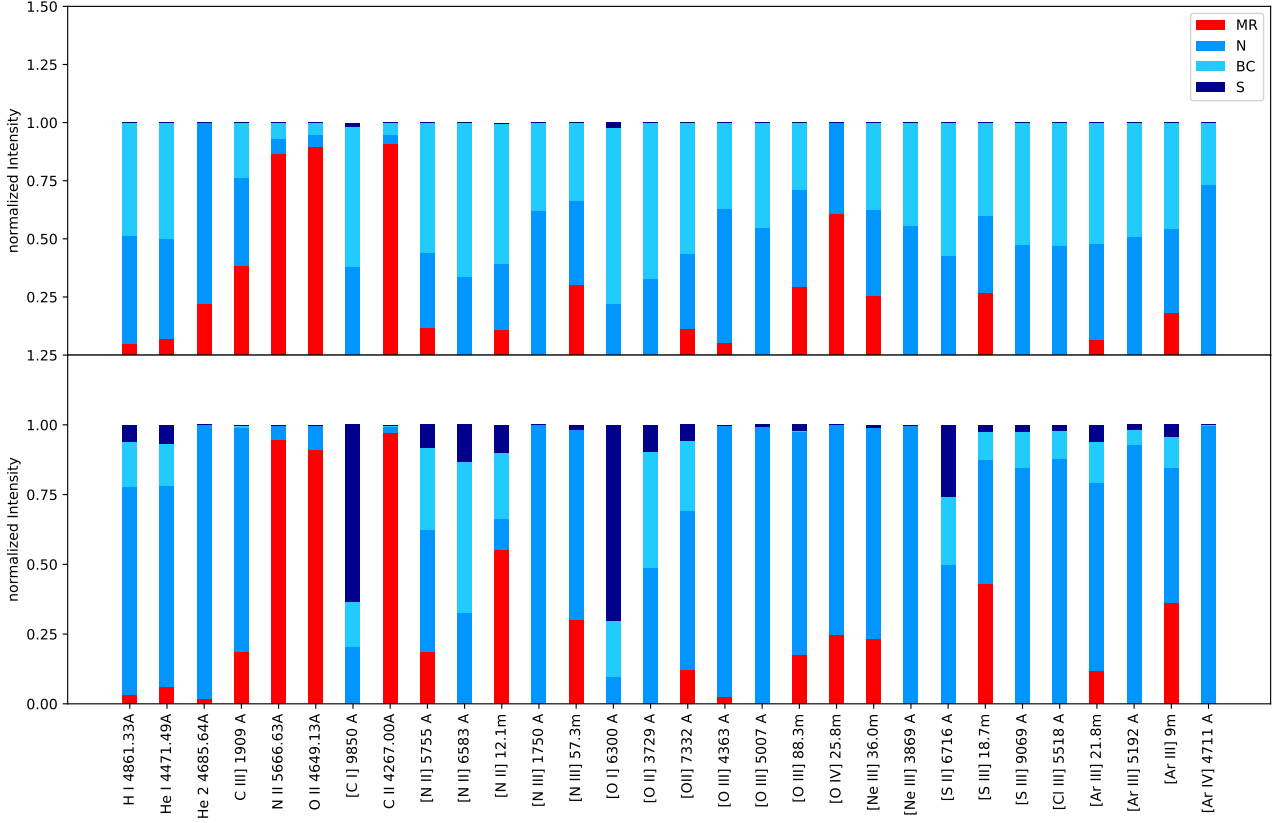


Figure 18. Normalized intensity of ORLs and CELs showing the contribution of the four components of the bi-abundance models (see sec. 2.5). Top panel represents the S₁ solution ($\log \text{ACF}(\text{O}) = 2.1$, and $\Omega/4\pi = 0.50$), and bottom panel the S₂ solution ($\log \text{ACF}(\text{O}) = 2.8$, and $\Omega/4\pi = 0.18$). The two solutions are selected from the two solution families shown in figure 17.

APPENDIX A: EMISSION LINES INTENSITIES OF THE TWO SOLUTIONS

In this appendix we present the line intensities obtained for the two solutions presented in Sec. 4, the second solution being in parenthesis. The intensities emitted by the 4 regions considered in each model are given, as well as the total intensities. Some recombination lines are not computed by Cloudy, we obtained them by calling PyNeb from pyCloudy through the `add_emis_from_pyneb` method (See Sec. 2 for details). These lines are identified with an asterisk. The recombination contribution to the [O III] 4363 emission line is not taken from Cloudy, but rather obtained by adding the radiative recombination and the dielectronic recombination, following Pequignot et al. (1991) and Nussbaumer & Storey (1984) respectively (See Sec. 5.3).

Table A1: Line intensities emitted by each of the four components (N , MR , BC , and S) and the total emission of our modeled bi-abundance nebula, for the S_1 , and S_2 solutions in parenthesis. Values are normalized to $H\beta$.

* Line intensities obtained using *PyNeb* (see sec. 2).

** The collisional contribution of this line is taken from *Cloudy*, the recombination contribution is obtained adding the radiative and dielectronic recombination from Pequignot et al. (1991) and Nussbaumer & Storey (1984), respectively (See Sec. 5.3).

Line	Normal	Rich clumps	Behind clumps	Shadow	Total
C II 1335.0 Å*	4.8e-3 (7.6e-3)	5.6e-2 (1.7e-1)	5.6e-3 (1.3e-3)	3.6e-6 (4.e-4)	6.7e-2 (1.8e-1)
[N III] 1746.82 Å	2.6e-3 (4.1e-3)	9.8e-8 (1.2e-7)	1.6e-3 (2.5e-7)	2.0e-8 (2.2e-6)	4.1e-3 (4.1e-3)
[N III] 1748.65 Å	5.4e-3 (8.5e-3)	2.2e-6 (2.5e-6)	3.2e-3 (5.2e-7)	4.2e-8 (4.6e-6)	8.5e-3 (8.5e-3)
[N III] 1749.67 Å	3.0e-2 (4.9e-2)	3.9e-6 (4.3e-6)	1.9e-2 (3.0e-6)	2.4e-7 (2.6e-5)	4.9e-2 (4.9e-2)
[N III] 1750.0 Å	6.2e-2 (9.8e-2)	9.2e-6 (1.0e-5)	3.7e-2 (6.1e-6)	4.8e-7 (5.3e-5)	9.9e-2 (9.8e-2)
[N III] 1752.16 Å	1.8e-2 (2.8e-2)	6.7e-7 (8.0e-7)	1.1e-2 (1.7e-6)	1.4e-7 (1.5e-5)	2.8e-2 (2.8e-2)
[N III] 1753.99 Å	5.6e-3 (8.8e-3)	2.4e-6 (2.7e-6)	3.4e-3 (5.5e-7)	4.4e-8 (4.8e-6)	8.9e-3 (8.9e-3)
C II 1761.0 Å*	1.1e-2 (1.8e-2)	1.2e-1 (3.5e-1)	1.3e-2 (3.e-3)	8.3e-6 (9.1e-4)	1.4e-1 (3.7e-1)
C III] 1909.0 Å	2.4e-1 (3.9e-1)	2.5e-1 (9.e-2)	1.5e-1 (4.9e-3)	1.2e-5 (1.3e-3)	6.5e-1 (4.9e-1)
C II 2837.0 Å*	1.8e-3 (2.9e-3)	2.1e-2 (6.4e-2)	2.1e-3 (4.9e-4)	1.4e-6 (1.5e-4)	2.5e-2 (6.7e-2)
Ne II 3218.19 Å*	3.1e-4 (4.9e-4)	4.7e-3 (3.7e-3)	3.2e-4 (—)	5.9e-8 (6.5e-6)	5.3e-3 (4.2e-3)
Ne II 3244.09 Å*	2.1e-4 (3.3e-4)	3.2e-3 (2.5e-3)	2.2e-4 (—)	4.0e-8 (4.4e-6)	3.6e-3 (2.9e-3)
Ne II 3334.83 Å*	5.e-4 (8.e-4)	7.1e-3 (5.6e-3)	5.2e-4 (—)	9.4e-8 (1.0e-5)	8.1e-3 (6.4e-3)
Ne II 3355.01 Å*	2.6e-4 (4.2e-4)	3.7e-3 (2.9e-3)	2.7e-4 (—)	4.9e-8 (5.4e-6)	4.2e-3 (3.3e-3)
Ne II 3360.59 Å*	1.0e-4 (1.6e-4)	1.5e-3 (1.2e-3)	1.1e-4 (—)	1.9e-8 (2.1e-6)	1.7e-3 (1.3e-3)
Ne II 3367.21 Å*	2.4e-4 (3.8e-4)	3.6e-3 (2.8e-3)	2.5e-4 (—)	4.5e-8 (5.e-6)	4.1e-3 (3.2e-3)
Ne II 3388.41 Å*	1.6e-4 (2.6e-4)	2.5e-3 (2.e-3)	1.7e-4 (—)	3.1e-8 (3.5e-6)	2.8e-3 (2.2e-3)
Ne II 3694.21 Å*	2.5e-4 (4.e-4)	3.1e-3 (2.5e-3)	2.6e-4 (—)	4.6e-8 (5.1e-6)	3.7e-3 (2.9e-3)
Ne II 3709.62 Å*	9.8e-5 (1.6e-4)	1.2e-3 (9.9e-4)	1.0e-4 (—)	1.8e-8 (2.e-6)	1.4e-3 (1.1e-3)
[O II] 3726.03 Å	1.6e-1 (2.6e-1)	— (—)	3.3e-1 (2.3e-1)	4.4e-4 (4.9e-2)	4.9e-1 (5.4e-1)
[O II] 3728.81 Å	9.9e-2 (1.6e-1)	— (—)	2.e-1 (1.3e-1)	2.8e-4 (3.1e-2)	3.e-1 (3.2e-1)
H I 3770.63 Å	1.9e-2 (3.e-2)	1.7e-3 (1.2e-3)	1.9e-2 (6.5e-3)	2.1e-5 (2.4e-3)	4.e-2 (4.e-2)
Ne II 3777.13 Å*	9.6e-5 (1.5e-4)	1.2e-3 (9.7e-4)	9.9e-5 (—)	1.8e-8 (2.e-6)	1.4e-3 (1.1e-3)
O II 3856.13 Å*	1.2e-5 (2.e-5)	2.5e-4 (2.4e-4)	1.3e-5 (—)	— (7.9e-7)	2.7e-4 (2.6e-4)
[Ne III] 3868.76 Å	4.4e-1 (7.e-1)	1.7e-4 (9.1e-5)	3.5e-1 (—)	1.8e-5 (2.e-3)	7.9e-1 (7.0e-1)
Ne III 3868.8 Å*	5.4e-1 (8.6e-1)	— (—)	4.3e-1 (—)	2.2e-5 (2.4e-3)	9.6e-1 (8.6e-1)
O II 3882.19 Å*	7.0e-5 (1.1e-4)	1.4e-3 (1.3e-3)	7.2e-5 (—)	4.0e-8 (4.4e-6)	1.5e-3 (1.4e-3)
He I 3888.63 Å	5.2e-2 (8.2e-2)	6.8e-3 (5.8e-3)	5.8e-2 (1.6e-2)	6.2e-5 (6.8e-3)	1.2e-1 (1.1e-1)
O II 3907.45 Å*	3.6e-5 (5.7e-5)	5.7e-4 (5.2e-4)	3.6e-5 (—)	2.e-8 (2.2e-6)	6.4e-4 (5.8e-4)
Ne III 3967.5 Å*	1.6e-1 (2.6e-1)	— (—)	1.3e-1 (—)	6.6e-6 (7.3e-4)	2.9e-1 (2.6e-1)
N II 4041.0 Å	4.8e-4 (7.7e-4)	9.7e-3 (2.e-2)	5.7e-4 (8.0e-7)	2.6e-7 (2.8e-5)	1.1e-2 (2.0e-2)
N II 4041.31 Å*	1.8e-4 (2.9e-4)	5.1e-3 (1.0e-2)	2.2e-4 (3.1e-7)	1.0e-7 (1.1e-5)	5.5e-3 (1.1e-2)
[S II] 4068.6 Å	1.0e-2 (1.6e-2)	1.4e-6 (7.9e-6)	1.3e-2 (5.3e-3)	4.4e-5 (4.9e-3)	2.3e-2 (2.7e-2)
O II 4069.88 Å*	4.9e-4 (7.8e-4)	7.2e-3 (6.7e-3)	5.e-4 (—)	2.7e-7 (3.e-5)	8.2e-3 (7.5e-3)
O II 4072.15 Å*	6.1e-4 (9.7e-4)	9.7e-3 (9.0e-3)	6.2e-4 (—)	3.4e-7 (3.7e-5)	1.1e-2 (1.0e-2)
[S II] 4076.35 Å	3.3e-3 (5.3e-3)	2.1e-7 (1.2e-6)	4.2e-3 (1.7e-3)	1.4e-5 (1.6e-3)	7.5e-3 (8.5e-3)
O II 4078.84 Å*	1.3e-4 (2.0e-4)	1.9e-3 (1.8e-3)	1.3e-4 (—)	7.0e-8 (7.7e-6)	2.2e-3 (2.e-3)
O II 4085.11 Å*	1.4e-4 (2.2e-4)	2.1e-3 (1.9e-3)	1.4e-4 (—)	7.6e-8 (8.4e-6)	2.3e-3 (2.1e-3)
O II 4087.15 Å*	1.0e-4 (1.6e-4)	2.1e-3 (1.9e-3)	1.0e-4 (—)	6.e-8 (6.6e-6)	2.3e-3 (2.1e-3)

Table A1: Continues

Line	Normal	Rich clumps	Behind clumps	Shadow	Total
O II 4089.29 Å*	2.e-4 (3.1e-4)	5.6e-3 (5.4e-3)	2.0e-4 (—)	1.2e-7 (1.3e-5)	6.0e-3 (5.8e-3)
O II 4092.93 Å*	8.3e-5 (1.3e-4)	1.3e-3 (1.2e-3)	8.5e-5 (—)	4.6e-8 (5.1e-6)	1.5e-3 (1.4e-3)
O II 4103.0 Å*	2.4e-5 (3.9e-5)	4.9e-4 (4.6e-4)	2.5e-5 (—)	1.4e-8 (1.5e-6)	5.3e-4 (5.0e-4)
O II 4104.99 Å*	1.0e-4 (1.7e-4)	2.2e-3 (2.1e-3)	1.1e-4 (—)	6.0e-8 (6.7e-6)	2.4e-3 (2.3e-3)
O II 4110.79 Å*	5.2e-5 (8.2e-5)	1.0e-3 (9.8e-4)	5.3e-5 (—)	3.e-8 (3.3e-6)	1.1e-3 (1.1e-3)
O II 4119.22 Å*	1.8e-4 (2.9e-4)	3.5e-3 (3.3e-3)	1.9e-4 (—)	1.1e-7 (1.2e-5)	3.9e-3 (3.6e-3)
O II 4120.28 Å*	1.7e-5 (2.8e-5)	3.1e-4 (2.9e-4)	1.8e-5 (—)	9.8e-9 (1.1e-6)	3.5e-4 (3.2e-4)
O II 4120.55 Å*	4.0e-5 (6.5e-5)	8.6e-4 (8.1e-4)	4.1e-5 (—)	2.3e-8 (2.6e-6)	9.4e-4 (8.8e-4)
O II 4121.46 Å*	7.6e-5 (1.2e-4)	1.3e-3 (1.3e-3)	7.8e-5 (—)	4.3e-8 (4.7e-6)	1.5e-3 (1.4e-3)
O II 4132.8 Å*	1.7e-4 (2.6e-4)	2.7e-3 (2.5e-3)	1.7e-4 (—)	9.3e-8 (1.0e-5)	3.1e-3 (2.8e-3)
O II 4140.7 Å*	6.1e-6 (9.7e-6)	1.0e-4 (9.3e-5)	6.2e-6 (—)	— (3.8e-7)	1.1e-4 (1.0e-4)
O II 4153.3 Å*	2.6e-4 (4.1e-4)	4.1e-3 (3.8e-3)	2.7e-4 (—)	1.4e-7 (1.6e-5)	4.7e-3 (4.2e-3)
O II 4156.53 Å*	3.2e-5 (5.2e-5)	5.4e-4 (5.e-4)	3.3e-5 (—)	1.8e-8 (2.0e-6)	6.0e-4 (5.5e-4)
O II 4169.22 Å*	7.5e-5 (1.2e-4)	1.2e-3 (1.1e-3)	7.7e-5 (—)	4.2e-8 (4.6e-6)	1.3e-3 (1.2e-3)
C III 4187.0 Å	1.3e-4 (2.2e-4)	2.8e-3 (1.0e-3)	1.1e-5 (—)	— (2.2e-8)	3.e-3 (1.2e-3)
O II 4189.79 Å*	2.1e-4 (3.3e-4)	7.2e-5 (6.8e-5)	2.1e-4 (—)	1.0e-7 (1.1e-5)	4.9e-4 (4.1e-4)
C II 4267.0 Å	1.3e-3 (2.1e-3)	2.7e-2 (8.4e-2)	1.5e-3 (3.8e-4)	1.1e-6 (1.2e-4)	3.0e-2 (8.7e-2)
O II 4317.14 Å*	1.4e-4 (2.3e-4)	2.3e-3 (2.1e-3)	1.5e-4 (—)	7.8e-8 (8.6e-6)	2.6e-3 (2.4e-3)
O II 4319.63 Å*	8.3e-5 (1.3e-4)	1.3e-3 (1.3e-3)	8.4e-5 (—)	4.5e-8 (5.e-6)	1.5e-3 (1.4e-3)
O II 4325.76 Å*	3.2e-5 (5.1e-5)	5.1e-4 (4.7e-4)	3.3e-5 (—)	1.8e-8 (1.9e-6)	5.7e-4 (5.3e-4)
O II 4336.86 Å*	5.9e-5 (9.5e-5)	9.5e-4 (8.8e-4)	6.0e-5 (—)	3.2e-8 (3.6e-6)	1.1e-3 (9.8e-4)
H I 4340.46 Å	2.2e-1 (3.5e-1)	2.0e-2 (7.6e-3)	2.3e-1 (7.6e-2)	2.5e-4 (2.8e-2)	4.7e-1 (4.6e-1)
O II 4345.56 Å*	1.8e-4 (2.8e-4)	2.8e-3 (2.6e-3)	1.8e-4 (—)	9.8e-8 (1.1e-5)	3.2e-3 (2.9e-3)
O II 4349.43 Å*	2.3e-4 (3.6e-4)	3.7e-3 (3.5e-3)	2.3e-4 (—)	1.3e-7 (1.4e-5)	4.2e-3 (3.9e-3)
[O III] 4363.0 Å**	3.e-2 (4.7e-2)	2.7e-3 (1.2e-3)	1.9e-2 (—)	6.6e-7 (7.3e-5)	5.1e-2 (4.9e-2)
O II 4366.89 Å*	1.5e-4 (2.4e-4)	2.4e-3 (2.2e-3)	1.5e-4 (—)	8.2e-8 (9.0e-6)	2.7e-3 (2.5e-3)
[N III] 4379.0 Å	7.5e-4 (1.2e-3)	2.1e-2 (8.e-3)	9.2e-5 (—)	— (1.5e-7)	2.2e-2 (9.2e-3)
O II 4414.9 Å*	1.2e-4 (1.9e-4)	1.5e-3 (1.4e-3)	1.2e-4 (—)	6.1e-8 (6.7e-6)	1.7e-3 (1.6e-3)
O II 4416.97 Å*	1.1e-4 (1.8e-4)	1.1e-3 (1.0e-3)	1.1e-4 (—)	5.6e-8 (6.1e-6)	1.3e-3 (1.2e-3)
He I 4471.49 Å	2.2e-2 (3.4e-2)	3.5e-3 (3.e-3)	2.5e-2 (7.3e-3)	2.9e-5 (3.2e-3)	5.e-2 (4.8e-2)
O II 4590.97 Å*	2.1e-4 (3.4e-4)	1.1e-4 (1.1e-4)	2.1e-4 (—)	1.0e-7 (1.1e-5)	5.4e-4 (4.5e-4)
N II 4607.16 Å*	7.3e-5 (1.2e-4)	9.3e-4 (1.9e-3)	8.5e-5 (1.1e-7)	3.4e-8 (3.7e-6)	1.1e-3 (2.0e-3)
N II 4613.87 Å*	4.6e-5 (7.4e-5)	5.9e-4 (1.2e-3)	5.4e-5 (7.0e-8)	2.2e-8 (2.4e-6)	6.9e-4 (1.3e-3)
N II 4621.39 Å*	7.7e-5 (1.2e-4)	9.5e-4 (1.9e-3)	9.e-5 (1.2e-7)	3.6e-8 (4.e-6)	1.1e-3 (2.1e-3)
N II 4630.54 Å*	2.8e-4 (4.5e-4)	3.8e-3 (7.8e-3)	3.3e-4 (4.3e-7)	1.3e-7 (1.5e-5)	4.4e-3 (8.3e-3)
O II 4638.86 Å*	3.2e-4 (5.1e-4)	4.3e-3 (4.e-3)	3.2e-4 (—)	1.7e-7 (1.9e-5)	5.e-3 (4.5e-3)
O II 4641.81 Å*	6.4e-4 (1.0e-3)	9.2e-3 (8.5e-3)	6.5e-4 (—)	3.5e-7 (3.8e-5)	1.0e-2 (9.6e-3)
N II 4643.09 Å*	1.e-4 (1.6e-4)	1.3e-3 (2.6e-3)	1.2e-4 (1.5e-7)	4.7e-8 (5.1e-6)	1.5e-3 (2.7e-3)
O II 4649.13 Å*	7.7e-4 (1.2e-3)	1.3e-2 (1.3e-2)	7.9e-4 (—)	4.3e-7 (4.8e-5)	1.5e-2 (1.4e-2)
C III 4650.25 Å	1.8e-4 (2.8e-4)	7.6e-5 (3.4e-5)	7.6e-7 (—)	— (9.2e-7)	2.5e-4 (3.2e-4)
O II 4650.84 Å*	3.4e-4 (5.4e-4)	4.6e-3 (4.3e-3)	3.4e-4 (—)	1.8e-7 (2.e-5)	5.3e-3 (4.8e-3)
O II 4661.63 Å*	3.6e-4 (5.7e-4)	4.8e-3 (4.5e-3)	3.6e-4 (—)	1.9e-7 (2.1e-5)	5.6e-3 (5.1e-3)
O II 4673.73 Å*	5.9e-5 (9.4e-5)	8.1e-4 (7.4e-4)	6.e-5 (—)	3.2e-8 (3.5e-6)	9.3e-4 (8.4e-4)
O II 4676.23 Å*	2.2e-4 (3.5e-4)	3.2e-3 (2.9e-3)	2.3e-4 (—)	1.2e-7 (1.3e-5)	3.6e-3 (3.3e-3)
He II 4685.64 Å	5.3e-2 (8.4e-2)	1.5e-2 (1.6e-3)	8.1e-5 (—)	1.9e-8 (2.1e-6)	6.7e-2 (8.5e-2)
O II 4696.35 Å*	2.7e-5 (4.3e-5)	3.6e-4 (3.3e-4)	2.7e-5 (—)	1.4e-8 (1.6e-6)	4.2e-4 (3.8e-4)
O II 4699.22 Å*	1.7e-5 (2.7e-5)	3.e-4 (2.8e-4)	1.7e-5 (—)	9.5e-9 (1.0e-6)	3.3e-4 (3.1e-4)
O II 4705.35 Å*	1.7e-5 (2.7e-5)	3.7e-4 (3.5e-4)	1.7e-5 (—)	1.e-8 (1.1e-6)	4.0e-4 (3.8e-4)
[Ar IV] 4711.26 Å	1.5e-2 (2.4e-2)	— (—)	5.5e-3 (—)	2.e-7 (2.2e-5)	2.1e-2 (2.4e-2)
[Ar IV] 4740.12 Å	1.1e-2 (1.8e-2)	— (—)	4.2e-3 (—)	1.5e-7 (1.6e-5)	1.5e-2 (1.8e-2)
N II 4779.72 Å*	5.2e-5 (8.2e-5)	8.3e-4 (1.7e-3)	6.1e-5 (8.2e-8)	2.6e-8 (2.9e-6)	9.5e-4 (1.8e-3)
N II 4788.13 Å*	6.9e-5 (1.1e-4)	1.2e-3 (2.4e-3)	8.2e-5 (1.1e-7)	3.5e-8 (3.9e-6)	1.3e-3 (2.5e-3)
N II 4803.29 Å*	1.3e-4 (2.1e-4)	2.3e-3 (4.7e-3)	1.6e-4 (2.1e-7)	6.7e-8 (7.4e-6)	2.6e-3 (5.e-3)
H I 4861.33 Å	4.7e-1 (7.4e-1)	4.8e-2 (3.4e-2)	4.9e-1 (1.6e-1)	5.4e-4 (6.e-2)	1.0e+0 (1.0e+0)

Table A1: Continues

Line	Normal	Rich clumps	Behind clumps	Shadow	Total
O II 4890.86 Å*	2.6e-5 (4.2e-5)	4.6e-4 (4.3e-4)	2.7e-5 (—)	1.5e-8 (1.6e-6)	5.1e-4 (4.7e-4)
O II 4924.53 Å*	1.4e-4 (2.2e-4)	2.1e-3 (2.e-3)	1.4e-4 (—)	7.5e-8 (8.3e-6)	2.4e-3 (2.2e-3)
O II 4943.0 Å*	8.6e-6 (1.4e-5)	2.e-4 (1.9e-4)	8.9e-6 (—)	— (5.6e-7)	2.2e-4 (2.e-4)
[O III] 4958.91 Å	1.8e+0 (2.8e+0)	9.7e-4 (5.e-4)	1.5e+0 (—)	1.9e-4 (2.1e-2)	3.2e+0 (2.8e+0)
[O III] 5006.84 Å	5.3e+0 (8.4e+0)	2.9e-3 (1.5e-3)	4.4e+0 (—)	5.6e-4 (6.2e-2)	9.6e+0 (8.5e+0)
[Ar III] 5191.82 Å	6.e-4 (9.5e-4)	— (—)	5.8e-4 (5.1e-5)	1.7e-7 (1.9e-5)	1.2e-3 (1.0e-3)
[N I] 5197.9 Å	2.3e-4 (3.7e-4)	1.8e-6 (1.2e-5)	7.1e-4 (1.2e-3)	5.1e-5 (5.6e-3)	9.9e-4 (7.2e-3)
[N I] 5200.26 Å	1.6e-4 (2.6e-4)	2.5e-7 (3.2e-6)	4.9e-4 (9.4e-4)	4.3e-5 (4.8e-3)	7.e-4 (6.e-3)
[Cl III] 5517.71 Å	4.2e-3 (6.6e-3)	— (—)	4.6e-3 (7.4e-4)	1.5e-6 (1.6e-4)	8.8e-3 (7.5e-3)
[Cl III] 5537.87 Å	4.7e-3 (7.6e-3)	— (—)	5.3e-3 (8.6e-4)	1.6e-6 (1.8e-4)	1.0e-2 (8.6e-3)
N II 5666.63 Å*	2.6e-4 (4.2e-4)	3.7e-3 (7.6e-3)	3.1e-4 (4.1e-7)	1.3e-7 (1.4e-5)	4.3e-3 (8.0e-3)
N II 5676.02 Å*	1.3e-4 (2.1e-4)	1.7e-3 (3.5e-3)	1.5e-4 (2.0e-7)	6.2e-8 (6.8e-6)	2.0e-3 (3.7e-3)
N II 5679.0 Å	4.4e-4 (7.1e-4)	5.3e-3 (1.1e-2)	5.2e-4 (6.9e-7)	2.2e-7 (2.4e-5)	6.2e-3 (1.1e-2)
N II 5679.56 Å*	4.7e-4 (7.5e-4)	7.7e-3 (1.6e-2)	5.5e-4 (7.4e-7)	2.3e-7 (2.5e-5)	8.7e-3 (1.7e-2)
N II 5686.21 Å*	7.8e-5 (1.2e-4)	1.0e-3 (2.1e-3)	9.1e-5 (1.2e-7)	3.7e-8 (4.1e-6)	1.2e-3 (2.2e-3)
N II 5710.77 Å*	9.4e-5 (1.5e-4)	1.3e-3 (2.7e-3)	1.1e-4 (1.5e-7)	4.5e-8 (5.e-6)	1.5e-3 (2.9e-3)
[N II] 5755.0 Å	6.9e-3 (1.1e-2)	2.4e-3 (4.7e-3)	1.2e-2 (7.4e-3)	1.9e-5 (2.1e-3)	2.1e-2 (2.5e-2)
He I 5875.64 Å	6.2e-2 (9.9e-2)	1.0e-2 (8.9e-3)	7.2e-2 (2.1e-2)	8.4e-5 (9.3e-3)	1.4e-1 (1.4e-1)
N II 5927.81 Å*	5.3e-5 (8.4e-5)	8.5e-4 (1.7e-3)	6.2e-5 (8.4e-8)	2.7e-8 (2.9e-6)	9.7e-4 (1.8e-3)
N II 5931.78 Å*	9.4e-5 (1.5e-4)	1.6e-3 (3.2e-3)	1.1e-4 (1.5e-7)	4.8e-8 (5.3e-6)	1.8e-3 (3.4e-3)
N II 5941.65 Å*	1.8e-4 (2.9e-4)	3.2e-3 (6.6e-3)	2.2e-4 (3.e-7)	9.4e-8 (1.0e-5)	3.6e-3 (6.9e-3)
N II 5952.39 Å*	2.8e-5 (4.4e-5)	4.7e-4 (9.5e-4)	3.3e-5 (4.5e-8)	1.4e-8 (1.5e-6)	5.3e-4 (1.e-3)
[O I] 6300.3 Å	8.3e-4 (1.3e-3)	— (1.7e-7)	2.9e-3 (2.7e-3)	8.7e-5 (9.5e-3)	3.8e-3 (1.4e-2)
[S III] 6312.06 Å	1.6e-2 (2.5e-2)	4.2e-7 (1.7e-6)	1.5e-2 (1.8e-3)	2.6e-6 (2.9e-4)	3.1e-2 (2.7e-2)
[N II] 6548.05 Å	1.5e-1 (2.4e-1)	2.0e-5 (5.1e-5)	3.e-1 (4.e-1)	8.9e-4 (9.8e-2)	4.5e-1 (7.4e-1)
H I 6562.81 Å	1.3e+0 (2.1e+0)	1.8e-1 (6.6e-2)	1.4e+0 (4.8e-1)	1.6e-3 (1.8e-1)	2.9e+0 (2.8e+0)
C II 6580.0 Å	1.1e-4 (1.8e-4)	7.6e-4 (2.2e-3)	1.3e-4 (2.7e-5)	7.5e-8 (8.2e-6)	1.0e-3 (2.4e-3)
[N II] 6583.45 Å	4.5e-1 (7.1e-1)	6.e-5 (1.5e-4)	8.8e-1 (1.2e+0)	2.6e-3 (2.9e-1)	1.3e+0 (2.2e+0)
He I 6678.15 Å	1.8e-2 (2.8e-2)	3.e-3 (2.5e-3)	2.0e-2 (6.e-3)	2.4e-5 (2.6e-3)	4.1e-2 (3.9e-2)
[S II] 6716.44 Å	3.3e-2 (5.3e-2)	2.5e-6 (9.9e-6)	4.4e-2 (2.6e-2)	2.5e-4 (2.7e-2)	7.7e-2 (1.1e-1)
[S II] 6730.82 Å	5.3e-2 (8.5e-2)	4.9e-6 (2.1e-5)	7.1e-2 (4.1e-2)	3.7e-4 (4.0e-2)	1.2e-1 (1.7e-1)
He I 7065.22 Å	1.4e-2 (2.3e-2)	1.3e-3 (1.2e-3)	1.6e-2 (3.8e-3)	1.4e-5 (1.5e-3)	3.2e-2 (2.9e-2)
[Ar III] 7135.79 Å	8.6e-2 (1.4e-1)	— (—)	9.8e-2 (1.8e-2)	5.7e-5 (6.2e-3)	1.8e-1 (1.6e-1)
C II 7231.0 Å*	1.8e-5 (2.8e-5)	2.8e-4 (8.7e-4)	2.1e-5 (5.0e-6)	1.4e-8 (1.6e-6)	3.2e-4 (9.0e-4)
[O II] 7332.0 Å	6.9e-3 (1.1e-2)	2.5e-3 (2.3e-3)	1.2e-2 (4.8e-3)	1.0e-5 (1.1e-3)	2.2e-2 (1.9e-2)
[S III] 9068.62 Å	2.9e-1 (4.6e-1)	1.3e-6 (4.0e-6)	3.2e-1 (7.1e-2)	1.2e-4 (1.3e-2)	6.1e-1 (5.5e-1)
[S III] 9530.62 Å	7.3e-1 (1.2e+0)	3.3e-6 (1.0e-5)	8.1e-1 (1.8e-1)	3.0e-4 (3.4e-2)	1.5e+0 (1.4e+0)
[C I] 9850.26 Å	3.5e-4 (5.5e-4)	— (2.5e-8)	5.5e-4 (4.3e-4)	1.5e-5 (1.7e-3)	9.1e-4 (2.7e-3)
He I 10830.3 Å	3.6e-1 (5.7e-1)	3.1e-2 (3.e-2)	3.9e-1 (9.0e-2)	3.2e-4 (3.5e-2)	7.8e-1 (7.2e-1)
[Ar III] 9.0 μm	8.5e-2 (1.4e-1)	4.3e-2 (1.0e-1)	1.1e-1 (3.1e-2)	1.1e-4 (1.2e-2)	2.4e-1 (2.8e-1)
[S IV] 10.5 μm	1.0e+0 (1.6e+0)	7.9e-1 (3.1e-1)	5.8e-1 (1.2e-6)	2.6e-5 (2.8e-3)	2.4e+0 (1.9e+0)
[N II] 12.2 μm	1.9e-3 (3.1e-3)	7.5e-4 (1.5e-2)	4.1e-3 (6.6e-3)	2.5e-5 (2.8e-3)	6.9e-3 (2.8e-2)
[Ne II] 12.8 μm	2.1e-2 (3.3e-2)	4.4e-2 (7.2e-1)	5.8e-2 (1.8e-1)	5.8e-4 (6.4e-2)	1.2e-1 (1.0e+0)
[Ne III] 15.6 μm	8.3e-1 (1.3e+0)	1.1e+0 (8.1e-1)	8.3e-1 (—)	1.4e-4 (1.5e-2)	2.8e+0 (2.1e+0)
[S III] 18.7 μm	3.6e-1 (5.7e-1)	2.9e-1 (5.5e-1)	4.3e-1 (1.3e-1)	2.8e-4 (3.0e-2)	1.1e+0 (1.3e+0)
[Ar III] 21.8 μm	5.4e-3 (8.7e-3)	8.4e-4 (1.5e-3)	6.8e-3 (1.9e-3)	6.8e-6 (7.5e-4)	1.3e-2 (1.3e-2)
[O IV] 25.9 μm	4.9e-1 (7.8e-1)	7.5e-1 (2.6e-1)	2.7e-4 (—)	— (8.7e-7)	1.2e+0 (1.0e+0)
[S III] 33.5 μm	1.4e-1 (2.3e-1)	1.4e-1 (2.5e-1)	1.7e-1 (4.2e-2)	1.1e-4 (1.2e-2)	4.5e-1 (5.4e-1)
[Ne III] 36.0 μm	7.3e-2 (1.2e-1)	5.1e-2 (3.6e-2)	7.4e-2 (—)	1.2e-5 (1.3e-3)	2.e-1 (1.5e-1)
[O III] 51.8 μm	7.9e-1 (1.3e+0)	5.9e-1 (3.1e-1)	6.1e-1 (—)	3.4e-4 (3.7e-2)	2.e+0 (1.6e+0)
[N III] 57.3 μm	3.5e-1 (5.5e-1)	2.9e-1 (2.5e-1)	3.2e-1 (3.7e-4)	1.3e-4 (1.4e-2)	9.6e-1 (8.1e-1)
[O III] 88.3 μm	1.7e-1 (2.7e-1)	1.2e-1 (6.e-2)	1.2e-1 (—)	6.9e-5 (7.6e-3)	4.1e-1 (3.4e-1)

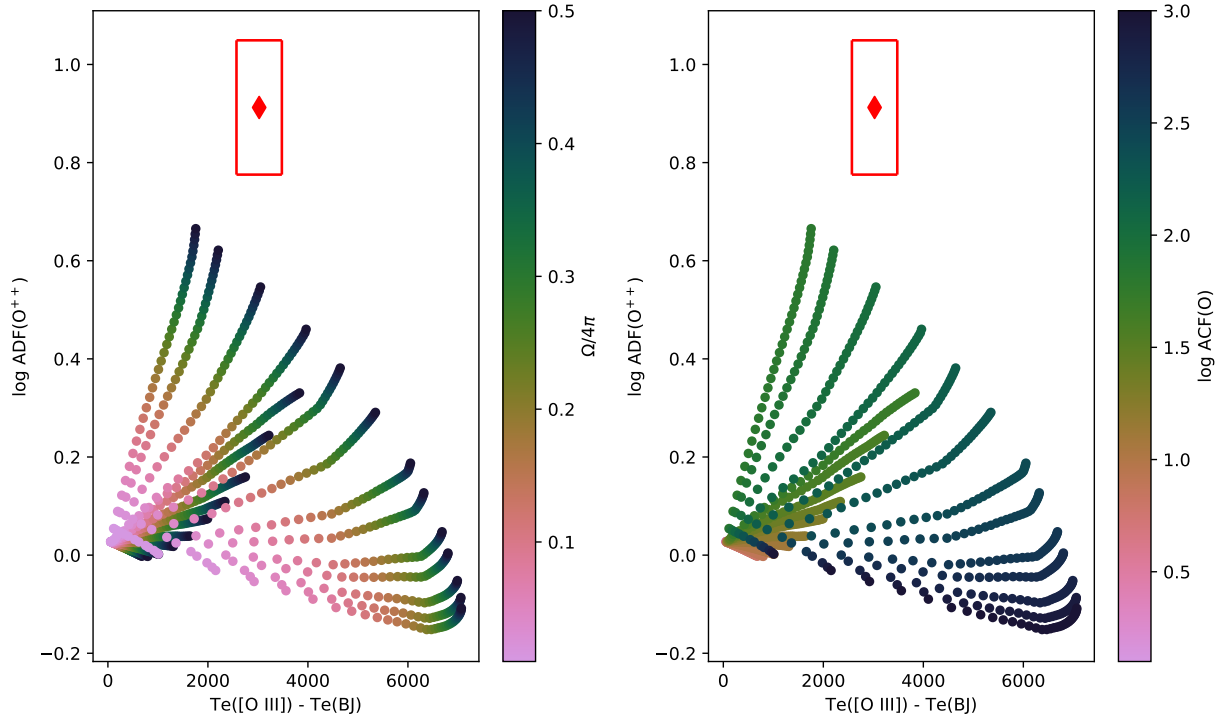


Figure B1. Relation between $\text{ADF}(\text{O}^{++})$ and $\text{T}([\text{O III}]) - \text{Te}(\text{BJ})$ for a sample of models where the helium in the *MR* component is enhanced in the same way as the metals.

This paper has been typeset from a $\text{T}_{\text{E}}\text{X}/\text{L}^{\text{A}}\text{T}_{\text{E}}\text{X}$ file prepared by the author.

APPENDIX B: THE HELIUM ABUNDANCE IN *MR* COMPONENT

In the main part of this paper, we present models where the helium abundance is locked to the hydrogen one. Here we explore an extreme case where the *MR* region is only H-poor and where helium is enhanced in the same way as the metals. We found that no solution can be determined in the $\text{ADF}(\text{O}^{++})$ vs ΔT observable space, as shown in fig. B1. A value of $\text{T}([\text{O III}]) - \text{Te}(\text{BJ})$ as high as the observed one can be obtained, but no high value for the $\text{ADF}(\text{O}^{++})$ can be reached (the maximum reached by the models is 5, while the observation is 8). This is mainly due to the fact that the *MR* region does not emit anymore the O II recombination lines: in the inner part of the *MR* region, where He is ionized (once or twice), the electron temperature is rather high due to the heating from this He ionizations (around 5,000K) and the recombination of O^{++} is strongly reduced. On the other side of the *MR* region, when He is recombined and does not heat anymore the gas, there is no photons anymore to ionize O^{+} into O^{++} , and no O II recombination lines can be produced. Nevertheless this cold region emits some continuum, leading to a low value for $\text{Te}(\text{BJ})$ and *in fine* to the observed $\text{T}([\text{O III}]) - \text{Te}(\text{BJ})$.

We explored another set of models where the He abundances is only enhanced by a fraction of the metal enhancement. We found that the maximal value for He/H that still leads to a marginal solution S3 that reproduces the observed $\text{ADF}(\text{O}^{++})$ and ΔT is: $\text{He}/\text{H} = 6.3$ (no solution is found for He/H higher than 6.3). The solution we obtain in this case corresponds to $\log \text{ACF} = 2.1$ and $\Omega/4\pi = 0.5$. The corresponding plot is shown in fig. B2. Intensities of He lines for this solution S3 are presented in B1, as well as the values for S1 and S2 presented in Sec. 4 and the observation from Yuan et al. (2011). We can see that for this high He content solution, the predictions of the He I lines are more or less 4 times higher than for the S1 and S2 solutions and are above the observed values. Regarding the He II line, this S3 solution is closer to the observation than the S1 or S2 values. We can conclude that He/H in the *MR* region is not well constraint by the model, being between 0.1 and 6, reminding that the enhancement in metals is of order of 125 for the S3 solution. We should also keep in mind that the ionized SED used in our models is a simple Planck function, adopting a more detailed atmosphere model being out of the scope of this paper.

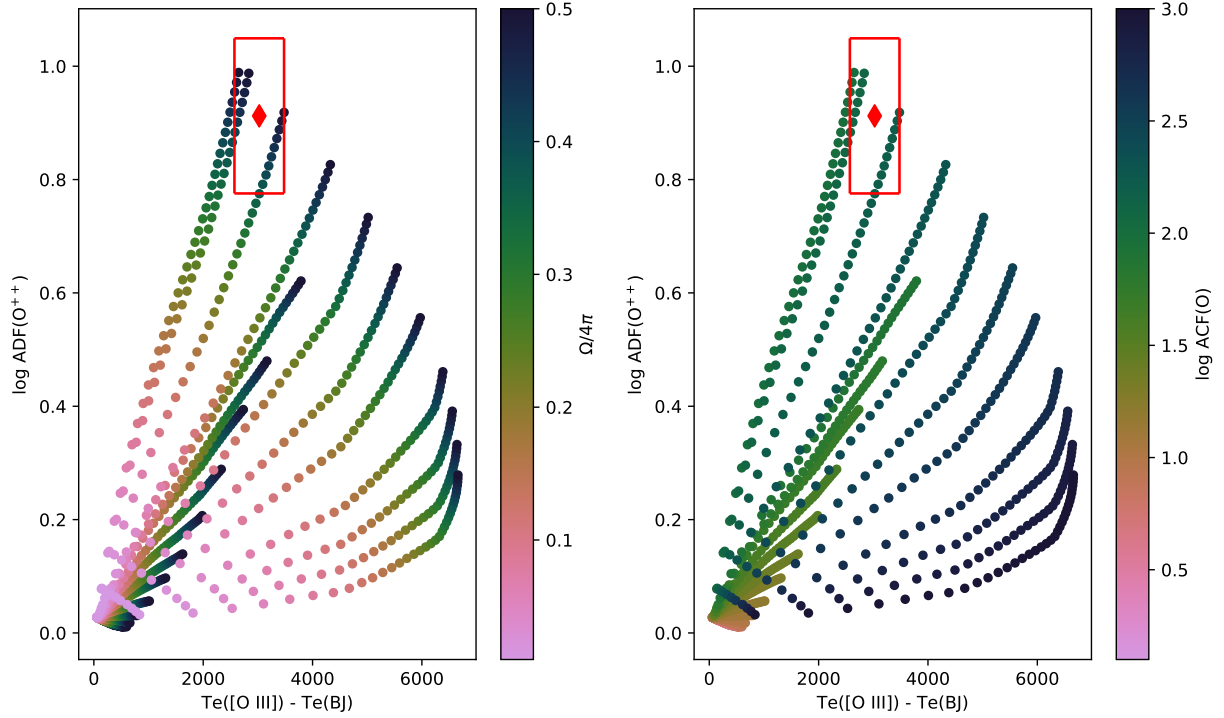


Figure B2. Relation between $\text{ADF}(\text{O}^{++})$ and $T([\text{O III}]) - T_e(\text{BJ})$ for a sample of models where the helium in the *MR* component is enhanced following this relation: $\text{He}/\text{H}_{MR} = \text{He}/\text{H}_N \times 0.5 (1 + \text{ACF}(\text{O}))$.

Table B1. Emission line intensities of He lines for the solution S3 with $\text{He}/\text{H} = 6.3$, $\log \text{ACF} = 2.1$, and $\Omega/4\pi = 0.5$. The observations for PN NGC 6153 from [Yuan et al. \(2011\)](#) and the solutions S1 and S2 of the paper are also shown.

Line	S1	S2	S3	Observation
He I 4471.49	5.0e-02	4.5e-02	1.9e-01	6.5e-02
He I 5875.64	1.4e-01	1.3e-01	5.7e-01	1.9e-01
He I 6678.15	4.1e-02	3.7e-02	1.6e-01	4.8e-02
He I 7065.22	3.2e-02	2.8e-02	8.4e-02	4.3e-02
He II 4685.64	6.8e-02	8.2e-02	1.0e-01	1.3e-01

Table B2. Physical parameters for each one of the four components, for the solution S₃.

	Normal	Rich clumps	Behind clumps	Shadow
$\langle T_e \rangle$ [K]	9653	2826	6913	6539
$\langle n_e \rangle$ [cm^{-3}]	2767	15570	2412	2670
$12 + \log(\text{O}/\text{H})$	8.75	10.85	8.75	8.75
$\Omega/4\pi^*$	0.50	0.50	0.50	0.50
H^+/H	0.99	1.00	0.96	0.97
O^+/O	0.08	0.36	0.96	0.66
O^{++}/O	0.85	0.64	0.00	0.31
O^{+3}/O	0.07	0.01	0.00	0.00
O mass (10^{-4}) [M_\odot]	6.6	7.5	5.8	1.2
Volume [10^{50}cm^{-3}]	345	3.2	306.3	64.2
% mass	44.2	8.3	39.3	8.2

* Fraction of solid angle for each component.